Journal of Petroleum Science and Engineering 214 (2022) 110506

Contents lists available at ScienceDirect

Journal of Petroleum Science and Engineering

journal homepage: www.elsevier.com/locate/petrol

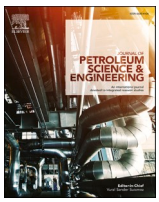

A fully coupled multidomain and multiphysics model considering stimulation patterns and thermal effects for evaluation of coalbed methane (CBM) extraction

Wai Li [a,*], Jishan Liu [a], Jie Zeng [a], Yee-Kwong Leong [a], Derek Elsworth [b], Jianwei Tian [a]

[a] School of Engineering, The University of Western Australia, Perth, WA, 6009, Australia
[b] Department of Energy and Mineral Engineering, G3 Centre and Energy Institute, The Pennsylvania State University, University Park, PA, 16802, USA

ARTICLE INFO

Keywords:
Coalbed methane
Stimulation
Multidomain
Multiphysics
Thermal effects

ABSTRACT

A deep understanding of the process of coalbed methane (CBM) extraction is of significance for both the unconventional energy supply and mine safety. The effects of stimulation patterns and thermal effects (including thermal shrinkage, non-isothermal sorption, and gas density change) significantly affect the CBM extraction process. Although thermal effects on CBM extraction have been investigated in previous studies, these effects have not been coupled with stimulation patterns, leading to an insufficient evaluation accuracy of previous models and a limited understanding of gas extraction in stimulated CBM reservoirs. This study developed a multidomain and multiphysics (thermal-hydraulic-mechanical, THM) model to fully couple different physical processes (including gas flow, coal deformation, gas desorption, and heat transfer) within a CBM reservoir framework considering various stimulation patterns to improve the simulation accuracy and obtain insights into CBM extraction. Three domains with distinct properties, i.e., the stimulated reservoir domain (SRD), non-stimulated reservoir domain (NSRD), and radial primary fracture (PF), were integrated into the CBM reservoir model to characterize the stimulation pattern. A group of partial differential equations (PDEs) was derived to characterize CBM transport within each domain and across different domain boundaries. A stimulated coalbed was defined as an assembly of three interacting porous media: coal matrix, continuous fractures (CF), and PF. The matrix and CF constituted a dual-porosity dual-permeability system, while the PF was simplified as a 1-D fractured medium. The finite element method (FEM) was employed to numerically solve the above PDEs. The proposed model was verified against two sets of field-measured CBM production data and compared to three previously published numerical models to reveal its advantage. The verified model was applied to investigate multidomain effects of stimulation treatment and evaluate the thermal effects of gas depletion on gas extraction in stimulated CBM reservoirs. The simulation results suggested (1) that the distinct properties of the different domains result in different permeability evolutions, which in turn influences CBM production; (2) that increasing the fracture complexity, enlarging the SRD size, and improving the SRD permeability with suitable stimulation techniques constitute effective approaches to enhance the CBM recovery; and (3) that ignoring thermal effects in CBM extraction can either overestimate or underestimate production, which mainly depends on the net effects of the thermal shrinkage strain and non-isothermal sorption during different production periods.

1. Introduction

In recent years, unconventional natural gas, including coalbed methane (CBM), shale gas, and tight gas, has received increasing attention as an important energy source (Tian et al., 2019; Li et al., 2020a; Zeng et al., 2020a; Zhang et al., 2020a). As an essential member of the unconventional natural gas family, CBM exhibits enormous reserves and has been commercially exploited in many countries, e.g., the USA, Australia, and China (Pan and Connell, 2012; Sun et al., 2018; Xia et al., 2019; Shi et al., 2020). Moreover, CBM pre-extraction from coalbeds is a vital method to prevent coal and gas outbursts so that mining practices can be safely conducted (Liu et al., 2014a; Liu and Cheng, 2015). Therefore, understanding the process of CBM extraction is not only of significance for the energy supply but also of significance for

* Corresponding author.
E-mail address: wai.li@research.uwa.edu.au (W. Li).

https://doi.org/10.1016/j.petrol.2022.110506
Received 20 October 2021; Received in revised form 24 February 2022; Accepted 8 April 2022
Available online 14 April 2022

mining safety. Due to the structural complexities of CBM reservoirs, a complicated flow process coupled with coal deformation, gas desorption, and thermal effects is expected to occur once extraction begins (Sun et al., 2018). Based on this consideration, many mathematical and physical models have been developed to predict the evolution of the methane flow rate and pressure in CBM reservoirs during gas extraction. Analytical models, which can be easily calculated, provide highly simplified methods to obtain benchmarks to better understand gas flow in CBM reservoirs (Clarkson and McGovern, 2005; Clarkson et al., 2007; Zeng et al., 2019). However, analytical models can hardly manage complex reservoir geometries and incorporate the interactions between multiple physical processes (such as coal deformation and temperature change during gas extraction) because these models usually employ linear-flow assumptions and experience mathematical difficulties in regard to irregular shapes (Zeng et al., 2021). In addition, analytical models cannot provide the real-time spatial distribution of certain key variables, such as the real gas pressure, dynamic porosity, and permeability (Wei et al., 2010; Sun et al., 2018; Zeng et al., 2020b; Li et al., 2020b). However, with the rapid development of numerical computation technology and computer hardware performance, it is possible to simulate dynamic changes in various physical quantities with calibrated numerical models fully coupling different physical processes (Gentzis and Bolen, 2008; Wei et al., 2010; Vishal et al., 2015; Zhang et al., 2016; Wei et al., 2021). Thus, the development of numerical models to accurately evaluate CBM production and provide detailed information on property evolution in CBM reservoirs has remained a highly attractive issue in the natural gas industry. Although great progress has been achieved in recent years, existing models should be improved to achieve accurate and precise prediction of CBM production and reservoir property evolution because specific processes and effects are often ignored in these models, which leads to undesirable prediction deviation. The complexities, physics, and coupling interactions previously ignored (or not fully considered) in earlier studies should be incorporated into an advanced numerical model to improve the simulation accuracy and enhance the knowledge of CBM extraction via a simulation investigation.

In CBM extraction modelling and simulation, a key issue is how to describe a stimulated coalbed with multiple domains. This issue originates from the fact that stimulation operations, such as hydraulic fracturing, always generate new domains with peculiar properties. Stimulation is usually conducted before CBM extraction so that the coalbed permeability near the borehole is significantly enhanced, and the effectiveness of CBM extraction is improved (Zhang et al., 2016). Recent advances in stimulation focus on the application of different stimulating techniques [e.g., high-energy gas fracturing (HEGF) and blasting (Zhu et al., 2012; Zhang et al., 2020b)] and innovative fracturing fluids [e.g., slickwater, nanoparticle-assisted fluids, and carbon dioxide (CO_2) (Cao et al., 2017a; Li et al., 2019a)]. These new techniques generally intensify the structural complexity of stimulated CBM reservoirs. For instance, the HEGF technique can create multi-wing primary artificial fractures instead of traditional double-wing fractures (Luo and Tang, 2015; Zhang et al., 2018), which has been confirmed in core tests and microseismic image observations (Germanovich et al., 1997; Craig and Blasingame, 2006; Chen et al., 2016). Another example is that the process of vibration and pressure wave transmission occurring in fracturing operations promote the activation of the original natural fractures into secondary fractures (with an increased aperture, porosity, permeability, and modified rock mechanical properties) in the area between primary artificial fractures (Brown et al., 2011; Yuan et al., 2015). This phenomenon is particularly obvious in high-impact operations such as deep-hole blasting and CO_2 fracturing (Liu et al., 2014b; Cao et al., 2017a). Based on these consequences of stimulation treatments, various stimulation patterns may be employed in different CBM reservoirs. Here, it is important to apply a suitable simplification method to describe different stimulation patterns so that the effects of these stimulation patterns on CBM production can be studied. Specifically, a stimulated CBM reservoir can be simplified as a multidomain assembly of porous continua (to represent the coal mass with both natural and activated fractures) and a 1-D discrete media (to represent the primary artificial fractures), as shown in Fig. 1 (choosing the top view of a vertical CBM wellbore as an example). As the most general scenario (referred to as the base scenario in this study), the stimulated coalbed contains multiple radial primary hydraulic fractures (PFs), a stimulated reservoir domain (SRD, defined as the coal body influenced by stimulation except PFs), and a non-stimulated reservoir domain (NSRD, defined as the coal body not influenced by stimulation), as shown in Fig. 1(a). Here, the SRD concept differs from the usual concept of the stimulated reservoir volume (SRV), which includes both PFs and the SRD. More specifically, the PF constitutes a simplification of a series of macroscale artificial fractures at the millimetre-level scale. The PF exhibits a much higher porosity and permeability and different mechanical properties than those of the original CBM reservoir. Although the PF is highly permeable, this fracture only accounts for a very small volumetric fraction of the entire reservoir. In contrast, the SRD, occupying a considerable fraction of the reservoir volume and including numerous activated micro-fractures (usually with a micrometre-level aperture), exhibits a higher porosity and permeability than those of the original CBM reservoir, although this enhancement is not as great as that observed for the PF. In addition, the pore compressibility of the SRD may differ from that of the original reservoir because of the activation of micro-fractures. Finally, occupying the remainder of the CBM reservoir, the NSRD retains all of the original coalbed properties. There occur natural fractures/cleats with sizes ranging from the nanometre level to the micrometre level in the NSRD, but the overall permeability of the NSRD is very low [ranging from the millidarcy level to the microdarcy level or even lower (Kou and Wang, 2020)]. The base scenario, as shown in Fig. 1(a), encompassing multiple PFs, the SRD and the NSRD, comprehensively covers most instances of producing CBM reservoirs. The base scenario can be reduced to the following scenarios via different settings corresponding to various actual conditions in CBM reservoirs: (1) If both the PF length and SRD volume are set to zero, the reservoir is considered not stimulated, as shown in Fig. 1(b). (2) If only one double-wing PF occurs, this can be simplified as two symmetrically distributed half-PFs (Settari and Cleary, 1984). In this case, the effects of secondary fractures can be ignored. The base scenario is then reduced into a case involving one double-wing PF and one NSRD, as shown in Fig. 1(c). (3) If there occur multiple primary radial primary fractures created along different directions, the base scenario can be reduced into a case with several (for example, three) double-wing PFs and one NSRD, as shown in Fig. 1(d). (4) In certain blasting cases, there exists no remarkable PF but only one SRD with many relatively homogeneous secondary fractures (Zhang et al., 2020b). Thus, the base scenario can be reduced into a case encompassing one SRD and one NSRD, as shown in Fig. 1(e). It should be mentioned that simplifying the CBM reservoir geometry based on the base scenario (multiple PFs + SRD + NSRD) depends on the stimulation treatment technique and consequences. For example, Cao et al. (2017a) and Zhang et al. (2018) reported that CBM reservoirs fractured with supercritical CO_2 could be regarded as entailing a stimulation pattern with multiple PFs, the SRD and the NSRD [Fig. 1(a)], while Chen et al. (2013) studied the process of gas extraction from coalbeds considering the NSRD concept [Fig. 1(b)]. Luo and Tang (2015) performed a pressure transient analysis based on the concept of multiple PFs and the NSRD [Fig. 1(d)]. In addition, Zhang et al. (2020b) proposed that certain CBM reservoirs subjected to blasting operations could be regarded as the SRD + NSRD pattern [Fig. 1(e)]. Therefore, the scenarios shown in Fig. 1(b), **(c)**, and **1(d)** can all be derived from the base scenario, as shown in Fig. 1(a). It is necessary to study the CBM extraction process under the five scenarios depicted in Fig. 1 to better understand and compare the effects of different stimulation patterns, while the base scenario is the most important case because the other scenarios are essentially the particular cases of the base scenario. In summary, a given stimulation pattern in CBM extraction could be

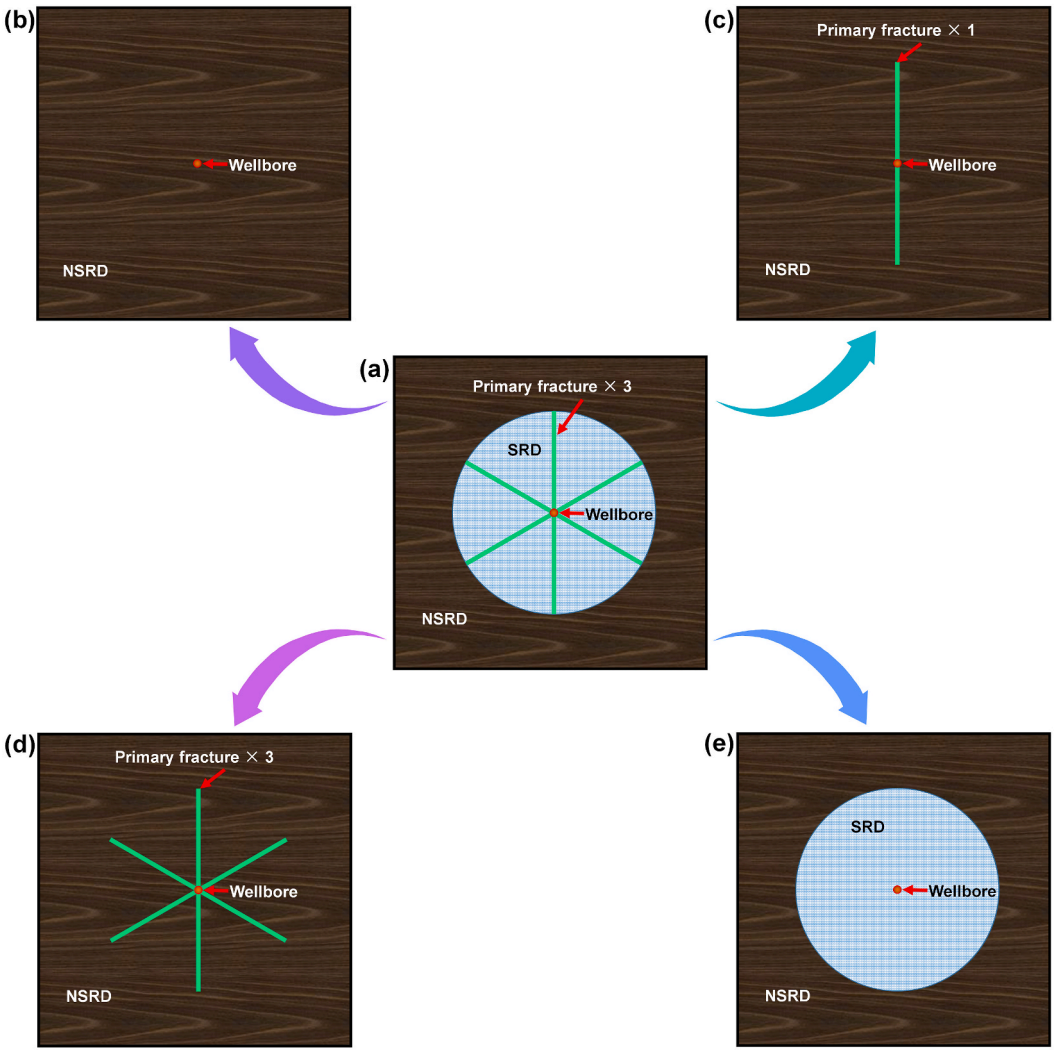

Fig. 1. Different scenarios of a producing CBM reservoir. (a) Base scenario: a stimulated CBM reservoir with multiple PFs, one SRD, and one NSRD. This scenario can be reduced into one of the following scenarios: (b) unstimulated CBM reservoir with only a producing well, (c) a hydraulically fractured CBM reservoir with a double-wing PF and one NSRD, (d) a stimulated CBM reservoir with 3 (double-wing) PFs and one NSRD, and (e) a stimulated CBM reservoir with one SRD and one NSRD.

regarded as a certain combination of the PF, SRD, and NSRD. As mentioned above, in previous CBM extraction modelling and simulation studies, the investigated stimulation patterns were usually limited to one type, while the performance of different stimulation patterns was seldom systematically analysed and compared.

CBM extraction involves a very complicated process not only because this process occurs in CBM reservoirs with a complex structure but also because this process is associated with multiple physical processes, including gas flow, coal deformation, gas desorption, and heat transfer (Li et al., 2016; Sun et al., 2018; Fan et al., 2019). Above all, the evolution of the porosity and permeability is a key issue in gas transport since these two physical quantities control gas storage and gas flow, respectively. Many previous studies have demonstrated that coal deformation influences the reservoir porosity and corresponding permeability of CBM reservoirs, which is caused by drawdown-induced effective stress evolution during gas extraction (Cui and Bustin, 2005; Shi and Durucan, 2004; Zhang et al., 2008; Pan and Connell, 2012; Peng et al., 2014; Liu et al., 2019). In addition, with decreasing gas pressure, gas is desorbed from the surface of coal matrix grains. This process not only supplies CBM to pores and fractures as a mass source of gas flow but also induces a certain sorption strain to affect the reservoir porosity and permeability.

The thermal effects of gas depletion during CBM extraction have often been ignored or not fully integrated into a framework with stimulation patterns. Classic reservoir modelling theories tend to assume that gas seepage in the reservoir entails isothermal flow. In contrast, temperature field evolution occurs during CBM extraction (Zhu et al., 2011; Qu et al., 2012; Li et al., 2016). This phenomenon can be attributed to four processes: (1) heat convection—gas flowing from the CBM reservoir towards the producing well removes heat; (2) heat conduction—the wellbore temperature is typically lower than that of the CBM reservoir (Li et al., 2016). Additionally, during CBM extraction, convection causes a colder area near the wellbore. This leads to a non-uniform temperature distribution throughout the whole reservoir, which promotes further heat conduction from the deep reservoir towards the wellbore; (3) heat desorption—gas desorption is an endothermic process resulting in system temperature reduction; (4) volumetric strain variation leads to energy change. The consequence of these four processes is that the low-temperature area near the wellbore is gradually enlarged with increasing gas depletion (Li et al., 2016; Sun et al., 2018). As a result, the decreasing temperature affects several key reservoir properties. First, temperature reduction results in thermal shrinkage of the coal matrix, directly influencing the porosity and thus the permeability. Second, temperature reduction hinders further desorption by maintaining a larger adsorbed gas amount than that under isothermal sorption (Qu et al., 2012; Li et al., 2016). Third, temperature

reduction alters the gas density to a certain degree based on the equation of state (EOS) of real gas. In summary, thermal effects should be fully coupled with other physical processes in the modelling and simulation of CBM reservoirs because the CBM extraction process is impacted by them in different aspects. Although the above thermal effects on CBM extraction have been included in previous modelling and simulation studies, these effects have not been integrated into a CBM reservoir model with stimulation patterns, leading to an insufficient evaluation accuracy of previous models and a limited understanding of gas extraction in stimulated CBM reservoirs (Zhu et al., 2011; Qu et al., 2012; Li et al., 2016; Sun et al., 2018). As mentioned above, a stimulated CBM reservoir usually contains multiple domains, which suggests that each of the aforementioned physical processes exhibits different behaviours and evolutions in these domains during CBM extraction due to the discrepancy in reservoir properties between the different domains. Therefore, to accurately simulate and evaluate gas extraction in stimulated CBM reservoirs, the abovementioned thermal effects (including thermal shrinkage, non-isothermal sorption, and non-isothermal gas density change) should be coupled with multiple complex physical processes (including gas flow, coal deformation, gas desorption, and heat transfer) and integrated into a CBM reservoir model comprising multiple domains (including the PF, SRD, and NSRD). Establishing, verifying, and applying such a model with high complexities with regard to physics and structure are challenging tasks.

This work focused on the development of a multidomain and multiphysics (thermal-hydraulic-mechanical, THM) model to fully couple different physical processes within a CBM reservoir framework considering various stimulation patterns to improve the simulation accuracy. Another focus was to gain insight into CBM extraction by applying the developed model. As an assembly of a dual-porosity-dual-permeability continuum and 1-D fractured media, a conceptual model with various domains, including the PF, SRD, and NSRD, was proposed to describe CBM reservoirs with different stimulation patterns. Based on the theories of poroelasticity, seepage mechanics, non-isothermal sorption, and heat transfer, a group of partial differential equations (PDEs) was derived to construct a fully coupled multidomain and multiphysics model. The finite element method (FEM) was employed to numerically solve the derived PDEs. The proposed model was verified against two sets of field-measured CBM production data and compared to three previously published numerical models to reveal its advantage. Subsequently, the verified model was applied to evaluate the effects of key influencing factors on CBM production, especially multidomain and thermal effects.

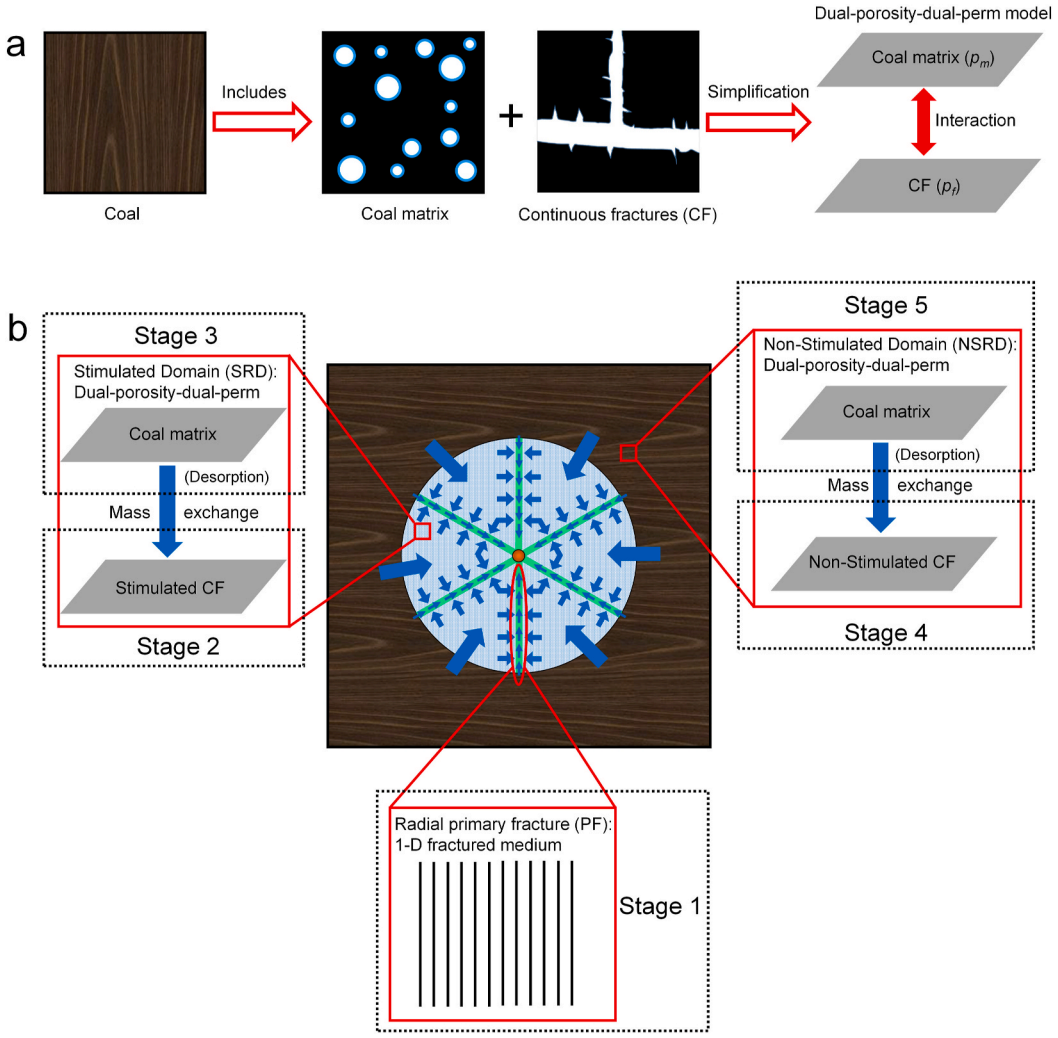

Fig. 2. Conceptual model. (a) Dual-porosity-dual-permeability model of coal with cleats/fractures. Coal consists of two porous media (coal matrix and CF) with different porosities, permeabilities, and mechanical properties. These media are further simplified as a pair of interacting and overlapping continua. p_m denotes the pressure in the coal matrix, while p_{CF} is the pressure in the CF. (b) Multiscale model, gas flow sequence, and domain division of the stimulated CBM reservoir. The blue arrows indicate the gas flow direction. (For interpretation of the references to colour in this figure legend, the reader is referred to the Web version of this article.)

2. Conceptual model

This section details the conceptual model and defines the corresponding multi-scale porous media, multiple domains, and sequential flow in gas extraction from stimulated CBM reservoirs.

2.1. Multiscale model and domain division

An illustration of the conceptual model is shown in Fig. 2. Coal is a typical dual-porosity medium in which a porous matrix provides nanometre-level pores accommodating CBM, while continuous fractures (CF) provide nanometre-to micrometre-level cleats and fissures as access pathways bridging matrix blocks (Wu et al., 2010a). Based on the theory of continuum mechanics, a dual-porosity-single-permeability model [considering that gas flow only occurs in fractures (Barenblatt et al., 1960; Warren and Root, 1963)] and a dual-porosity-dual-permeability model [considering the matrix and CF as two interacting porous systems (Elsworth and Bai, 1992; Bai and Elsworth, 2000; Wu et al., 2010a)] have been developed and successfully applied to characterize CBM reservoirs. The advantage of the dual-porosity-dual-permeability model over the dual-porosity-single-permeability model is that the former model relies on two interacting pore-pressure systems (instead of a single pore-pressure system) to reflect the effects of the stark difference between matrix and CF properties [i.e., the reservoir heterogeneity; please refer to Bai et al. (1997) and Chen et al. (2013)] on the gas flow. Therefore, the present work employed a dual-porosity-dual-permeability model to describe the bulk coalbed (without PFs) as two overlapping continua with different porosities, permeabilities, and mechanical properties, as shown in Fig. 2(a).

According to the introduction in Section 1, stimulation treatment creates abundant new/activated fractures, which results in an enhanced porosity, higher permeability, and different mechanical properties of the CF in the SRD over those of the CF in the NSRD, while the properties of the matrices in the SRD and NSRD are considered identical. In addition, the PF is abstracted as a 1-D fractured medium with a greatly enhanced porosity, higher permeability, and different pore compressibility than those of the original CBM reservoir to bridge the coal mass and the producing well. In summary, three media are defined (the coal matrix, CF, and PF) jointly exhibiting multi-scale characteristics, and there are three domains (the SRD, NSRD, and PF) reflecting the multidomain features of a given stimulated CBM reservoir.

2.2. Flow sequence

Based on the defined multi-scale model and domain division, a sequential flow process including five flow stages was considered to describe gas transport in the stimulated CBM reservoir, as illustrated in Fig. 2(b): at the beginning of gas extraction, the original gas in the PFs very quickly flowed towards the wellbore due to the notable difference between the bottom-hole and initial reservoir pressures (Stage 1). The significantly depleted pressure in the PFs then induced the free gas in the CF of the SRD to flow into the PFs (Stage 2). Subsequently, the pressure difference (which can also be equivalently expressed as the concentration difference, as described in Section 3.2) between the CF and coal matrix caused mass exchange. As a mass source, the coal matrix supplied gas to the CF via diffusion, and gas desorption occurred with pressure reduction in the matrix (Stage 3). Moreover, gas in the CF of the NSRD started flowing into the CF of the SRD to maintain the gas flow continuity, which was caused by the pressure difference between the SRD and NSRD (Stage 4). Finally, gas in the matrix of the NSRD diffused into the CF of the NSRD, and gas desorption occurred in the matrix of the NSRD (Stage 5). Previously, several multidomain sequential flow models have been successfully applied in unconventional gas extraction simulations. Peng et al. (2015) proposed a multidomain model to describe the gas transport behaviour in shale gas reservoirs, but the SRD and NSRD were not differentiated in their study. Li et al. (2019b, 2020b) and Cui et al. (2020) studied the process of shale gas production with multidomain models differentiating the SRD and NSRD, but their works remained limited to shale reservoirs and horizontal wells with one primary hydraulic fracture in each fracturing segment. In this work, we extended multidomain sequential flow to the CBM extraction process with a vertical wellbore and an SRD containing multiple PFs.

As previously mentioned, in addition to gas flow, coal deformation, gas desorption, and thermal effects should be incorporated into the model. In the next section, the mathematical model capturing these physical processes in the different media/domains and interactions between these processes and media/domains are detailed.

3. Mathematical model

The mathematical model formulation is based on the following assumptions: (1) the coal matrix, CF, and PF are deemed isotropic and linear-elastic; (2) gas flow entails a single-phase process, i.e., the impact of water in the CBM reservoir is ignored; (3) the CBM reservoir is saturated with methane in the initial state; (4) mechanical deformation is much smaller than the volume of coal block; (5) gas transport in the coal matrix and CF are driven by seepage, while the mass exchange between the matrix and CF is controlled by diffusion (Chen et al., 2013; Li et al., 2016; Fan et al., 2019). (6) The gas supply attributed to desorption is only considered in the matrix because the matrix contains the majority of the solid coal grains. (7) Coal deformation instantly reaches local mechanical equilibrium conditions, i.e., a certain pressure distribution corresponds to one effective strain distribution (Chen et al., 2013; Peng et al., 2015). (8) The heat transfer process instantly reaches local thermal equilibrium conditions, i.e., a certain pressure distribution corresponds to one temperature distribution (Li et al., 2016; Fan et al., 2019).

3.1. Mechanical coupling equations

First, the whole CBM reservoir obeys the following stress-strain relationship based on Biot's poroelasticity theory and the dual-porosity assumption (Detournay and Cheng, 1993; Zhang et al., 2008; Peng et al., 2015; Cao et al., 2016a; Li et al., 2016, 2019b, 2020b; Fan et al., 2019):

$$\varepsilon_{ij}=\frac{(1+\upsilon)}{3K(1-2\upsilon)}\sigma_{ij}-\frac{\upsilon}{3K(1-2\upsilon)}\sigma_{kk}\delta_{ij}+\frac{\alpha_{CF}p_{CF}}{3K}\delta_{ij}+\frac{\alpha_m p_m}{3K}\delta_{ij}+\frac{\alpha_T T}{3}\delta_{ij}+\frac{\varepsilon_s}{3}\delta_{ij} \tag{1}$$

where ε_{ij} is a component of the total strain tensor, ν is the bulk Poisson ratio of coal, K is the bulk volumetric modulus of coal, T is the temperature, $\sigma_{kk}=\sigma_{11}+\sigma_{22}+\sigma_{33}$ denotes the total stress, with σ_{11}, σ_{22} and σ_{33} the normal stresses along the three axial directions of the spatial coordinate system, δ_{ij} is the Kronecker delta, which equals 1 for $i=j$ and 0 for $i\neq j$, ε_s is the non-isothermal sorption-induced volumetric strain, and p_{CF} and p_m denote the gas pressures in the CF and coal matrix, respectively. α_{CF} and α_m are the effective Biot coefficients of the CF and coal matrix, respectively. These quantities can be determined with the following equations:

$$\begin{cases}\alpha_{CF}=\dfrac{\gamma_{CF}K\alpha^*_{CF}}{K_{CF}}\\ \alpha_m=\dfrac{\gamma_m K\alpha^*_m}{K_m}\end{cases} \tag{2}$$

where γ_{CF} and γ_m are the volumetric fractions occupied by the CF and coal matrix, respectively, and $\gamma_{CF}+\gamma_m=1$. K_{CF} and K_m are the individual bulk moduli of the CF and coal matrix, respectively. α^*_{CF} and α^*_m are the individual Biot coefficients of the CF and coal matrix, respectively. γ_{CF}, γ_m, K_{CF}, K_m, α^*_{CF} and α^*_m can be estimated/determined via core analysis (Mehrabian and Abousleiman, 2015; Cao et al., 2016a; Li et al., 2020b)

and/or acoustic measurements (Mehrabian and Abousleiman, 2015; Rezaee, 2015). α_T denotes the thermal expansion coefficient of coal.

Note that K and ν in Eq. (1) are volume-weighted quantities (Cao et al., 2016a; Berryman, 2002):

$$\frac{1}{K}=\frac{\gamma_{CF}}{K_{CF}}+\frac{\gamma_m}{K_m} \tag{3}$$

$$\upsilon=\gamma_m\upsilon_m+\gamma_{CF}\upsilon_{CF} \tag{4}$$

where υ_m and υ_{CF} are the individual Poisson ratios of the CF and coal matrix, respectively.

The non-isothermal sorption-induced volumetric strain ε_s is related to the changing temperature and can be obtained with the following modified Langmuir-type sorption equation (Zhu et al., 2011):

$$\varepsilon_s=\frac{\varepsilon_L p_m}{p_m+P_L}F(p_m,T) \tag{5}$$

where ε_L is the Langmuir sorption strain constant, while P_L is the Langmuir pressure constant of coal. $F(p_m,T)$ is a function reflecting the temperature dependence of the gas sorption amount, which is defined by the following equation based on the van 't Hoff equation (Busch and Gensterblum, 2011; Zhu et al., 2011; Li et al., 2016):

$$F(p_m,T)=\exp\left[-\frac{d_2}{1+d_1p_m}\left(T-T_{ref}\right)\right] \tag{6}$$

where d_1 is a pressure coefficient, d_2 is a temperature coefficient, and T_{ref} is the reference temperature of the desorption test. According to Eq. (5), given the same p_m value, a higher T value corresponds to a lower ε_s value.

On the right-hand side of Eq. (1), the first and second terms denote the mechanical strains induced by the stress tensor along the normal and shear directions, respectively. The third and fourth terms denote the strains caused by the gas pressure in the CF and coal matrix, respectively. The fifth term is the contribution of thermal expansion/shrinkage, and the final term is the contribution of sorption-induced strain to the total strain tensor. Furthermore, according to the strain-displacement relationship (the Cauchy equation) and stress equilibrium relationships (Detournay and Cheng, 1993; Zhang et al., 2008), we can obtain the following:

$$\begin{cases}\varepsilon_{ij}=\dfrac{1}{2}\left(u_{i,j}+u_{j,i}\right)\\ \sigma_{ij,j}+f_i=0\end{cases} \tag{7}$$

where u_i is the displacement along the i direction, σ_{ij} is a component of the total stress tensor, and f_i is the body force along the i direction, with i, $j = x, y, z$. Combining Eqs. (1) and (7) yields the Navier-Cauchy-type deformation equation as the governing equation of the strain field (Zhu et al., 2011) as follows:

$$\frac{3K(1-2\upsilon)}{2(1+\upsilon)}u_{i,kk}+\frac{3K}{2(1+\upsilon)}u_{k,ki}-\alpha_{CF}p_{CF,i}-\alpha_m p_{m,i}-K\alpha_T T_{,i}-K\varepsilon_{s,i}+f_i=0 \tag{8}$$

Eq. (8) represents a strict mathematical form to fully couple mechanical deformation, effects of gas pressure evolution in the coal matrix and CF, thermal expansion/shrinkage, and sorption-induced strain.

3.2. Gas transport in the coal matrix

In this section, the governing equations for mass transfer in the coal matrix are derived. Based on the mass conservation law, the general equation for gas transport in the coal matrix can be written as (Chen et al., 2013; Li et al., 2016):

$$\frac{\partial m_m}{\partial t}+\nabla\cdot\left(-\rho_{gm}\frac{k_{m,stress}}{\mu}\nabla p_m\right)=-Q_{m-CF} \tag{9}$$

where m_m denotes mass storage of gas in the coal matrix, ρ_{gm} is the gas density in the coal matrix, $k_{m,stress}$ denotes the stress-dependent permeability of the coal matrix, μ is the methane viscosity, and $-Q_{m\text{-}CF}$ denotes the mass sink term offering gas from the coal matrix to the CF. Furthermore, m_m equals the mass sum of free and adsorbed gas in the coal matrix:

$$m_m=\rho_{gm}\varphi_{m,stress}+\rho_a\rho_s V_{ads} \tag{10}$$

where $\varphi_{m,stress}$ is the stress-dependent matrix porosity considering the impact of coal deformation, ρ_a is the methane density under standard conditions, i.e., 0.717 kg/m^3 (Zhang et al., 2008), ρ_s is the bulk density of coal, and V_{ads} is the adsorption volume per unit of coal mass as the standard gas volume, which can be obtained via a modified Langmuir-type equation with a similar form to that of Eq. (5), considering the temperature dependence of gas sorption (Zhu et al., 2011; Qu et al., 2012):

$$V_{ads}=\frac{V_L p_m}{P_L+p_m}F(p_m,T) \tag{11}$$

where V_L denotes the Langmuir volume constant of coal. Give the same p_m value, a higher T value corresponds to a lower V_{ads} value.

To obtain an exact expression of $\varphi_{m,stress}$ in Eq. (10), the influence of the effective stress should be considered. The evolution of the stress-dependent matrix porosity during gas extraction can be expressed as the following general form proposed in previous works (Liu et al., 2011; Wei et al., 2018):

$$\varphi_{m,stress}=\varphi_{m0}+\alpha_m^*(\varepsilon_{em}-\varepsilon_{em0}) \tag{12}$$

where ε_{em} is the effective strain at a certain time point, while ε_{em0} is the effective strain in the coal matrix under the initial conditions. These quantities are defined as (Qu et al., 2012):

$$\varepsilon_{em}=\varepsilon_v+\frac{p_m}{K_m}-\varepsilon_s-\alpha_T T \tag{13}$$

$$\varepsilon_{em0}=\varepsilon_{v0}+\frac{p_{m0}}{K_m}-\varepsilon_{s0}-\alpha_T T_0 \tag{14}$$

where the bulk volumetric strain $\varepsilon_v=\sigma_{kk}/K$ can be numerically obtained by solving the mechanical coupling equation [Eq. (8)], K_m is the bulk modulus of the coal matrix, ε_{v0} is the initial bulk volumetric strain, which can be obtained by numerically solving Eq. (8) under the initial and boundary conditions, and ε_{s0} is the initial sorption-induced strain. Combining Eqs. (12)–(14) yields the following:

$$\begin{aligned}\varphi_{m,stress}&=\varphi_{m0}+\alpha_m^*\left[(\varepsilon_v-\varepsilon_{v0})+\frac{(p_m-p_{m0})}{K_m}-(\varepsilon_s-\varepsilon_{s0})-\alpha_T(T-T_0)\right]\\&=\varphi_{m0}+\alpha_m^*(\varepsilon_v-\varepsilon_{v0})+\frac{\alpha_m^*(p_m-p_{m0})}{K_m}-\alpha_m^*(\varepsilon_s-\varepsilon_{s0})-\alpha_m^*\alpha_T(T-T_0)\end{aligned} \tag{15}$$

On the right-hand side of Eq. (15), the second term is the matrix porosity change resulting from the variation in the bulk volumetric strain, the third term is the porosity change caused by the variation in the gas pressure in the matrix, the fourth term is the matrix porosity change due to the variation in the sorption-induced strain, and the fifth term is the matrix porosity change attributed to the variation in thermal strain. This general porosity model is based on triaxial strain conditions. Zhang et al. (2008) demonstrated that this model could be reduced to the classic Palmer and Mansoori model (Palmer and Mansoori, 1998) by applying uniaxial conditions. This model, along with its various modified forms, has been successfully applied in modelling and simulating the gas extraction process in unconventional reservoirs (Zhang et al., 2008; Wu et al., 2010a; Wei et al., 2018; Cui et al., 2018).

As the relationship between the porosity and permeability, the cubic law is employed to obtain the matrix permeability ($k_{m,\ stress}$) affected by the effective stress (Pan and Connell, 2012):

$$k_{m,stress} = k_{m0}\left(\frac{\varphi_{m,stress}}{\varphi_{m0}}\right)^3 \tag{16}$$

where k_{m0} is the initial permeability of the coal matrix.

Regarding porous medium i (i = m, CF, PF), the gas density ρ_{gi} can be obtained with the equation of state of real gas:

$$\rho_{gi} = \frac{Mp_i}{Z_i RT} \tag{17}$$

where M is the molar weight of methane, i.e., 0.016 kg/mol, R is the universal gas constant, namely, 8.314 J/(mol·K), p_i is the gas pressure in medium I, and Z_i is the deviation factor of real gas, which can be obtained with the following empirical expression (Mahmoud, 2014):

$$Z_i = 0.702\left(p_{pri}\right)^2 \exp\left(-2.5T_{pr}\right) - 5.524p_{pri}\exp\left(-2.5T_{pr}\right) + 0.044\left(T_{pr}\right)^2 - 0.164T_{pr} + 1.15 \tag{18}$$

where $p_{pri} = p_i/p_c$ is the pressure ratio and p_c is the critical pressure of methane, i.e., 4.6×10^6 Pa. $T_{pr} = T/T_c$ is the temperature ratio, and T_c is the critical temperature of methane, namely, 190.74 K.

An approach based on An et al. (2013), Xia et al. (2015), and Li et al. (2016) was selected to determine the sink term of the matrix ($Q_{m\text{-}CF}$). The key idea of this approach was to describe the gas diffusion process (i.e., a process driven by a gas concentration difference) from the coal matrix towards the CF considering the characteristic time (τ_0):

$$Q_{m-CF} = \frac{\rho_m - \rho_{CF}}{\tau_0} = \frac{M}{RT\tau_0}\left(\frac{p_m}{Z_m} - \frac{p_{CF}}{Z_{CF}}\right) \tag{19}$$

where ρ_{CF} is the gas density in the CF, p_{CF} is the gas pressure in the CF, and Z_{CF} is the deviation factor of real gas in the CF. τ_0 can be experimentally assessed or determined via the following expression (Chen et al., 2013):

$$\tau_0 = \frac{1}{D_{m-CF}\delta} \tag{20}$$

where $D_{m\text{-}CF}$ is the diffusivity of methane in the matrix, while δ is a shape factor. $D_{m\text{-}CF}$ can be approximately expressed in the following form (Kranz et al., 1990; Chen et al., 2013):

$$D_{m-CF} = \frac{k_{m,stress}}{\varphi_{m,stress}\mu\beta} \tag{21}$$

where β is the compressibility of methane. According to the definition of the gas compressibility, β can be expressed as:

$$\beta = -\frac{1}{\rho_{gm}}\cdot\left(\frac{\partial\rho_{gm}}{\partial p_m} + \frac{\partial\rho_{gm}}{\partial T}\right) = -\left(\frac{1}{p_m} - \frac{1}{Z_m}\cdot\frac{\partial Z_m}{\partial p_m} - \frac{1}{T} - \frac{1}{Z_m}\cdot\frac{\partial Z_m}{\partial T}\right) \tag{22}$$

where $\frac{\partial Z_m}{\partial p_m}$ and $\frac{\partial Z_m}{\partial T}$ can be directly calculated according to Eq. (18). Note that the first minus sign on the right-hand side ensures that the value of β is positive. This form of β not only reflects the gas expansion effect with a small increase in temperature but also reflects the gas compression effect with a small increase in pressure. The exact value of β based on Eq. (18) is the net result of these two competitive effects. Therefore, substituting Eq. (22) into Eq. (21) yields an exact expression of the diffusivity of methane in the matrix:

$$D_{m-CF} = \frac{k_{m,stress}}{\varphi_{m,stress}\mu\left(\frac{1}{Z_m}\cdot\frac{\partial Z_m}{\partial p_m} - \frac{1}{p_m} + \frac{1}{T} + \frac{1}{Z_m}\cdot\frac{\partial Z_m}{\partial T}\right)} \tag{23}$$

In addition, the shape factor δ can be obtained with the following equation (Lim and Aziz, 1995; Van Heel et al., 2008; Teng et al., 2018; Fan et al., 2019):

$$\delta = \frac{3\pi^2}{L_m^2} \tag{24}$$

where L_m is the cleat spacing (i.e., the width of a single cubic matrix block). Here, L_m is considered an average constant since the deformation of the matrix is lower than that of the coal block, and the effect of deformation on the characteristic time τ_0 can be ignored. Combining Eqs. (19), (20), (23) and (24) results in an exact expression of the sink term for the coal matrix:

$$Q_{m-CF} = \frac{3\pi^2 M k_{m,stress}\left(\frac{p_m}{Z_m} - \frac{p_{CF}}{Z_{CF}}\right)}{L_m^2 RT\varphi_{m,stress}\mu\left(\frac{1}{Z_m}\cdot\frac{\partial Z_m}{\partial p_m} - \frac{1}{p_m} + \frac{1}{T} + \frac{1}{Z_m}\cdot\frac{\partial Z_m}{\partial T}\right)} \tag{25}$$

Substituting Eqs. (10) and (11) and (15)–(17) and (25) into Eq. (9) yields the overall governing equation for the coal matrix:

$$\begin{cases} \dfrac{\partial\left(\rho_{gm}\varphi_{m,stress} + \dfrac{\rho_a\rho_s V_L p_m}{P_L + p_m}F(p_m,T)\right)}{\partial t} + \nabla\cdot\left(-\dfrac{Mp_m k_{m,stress}}{Z_m RT\mu}\nabla p_m\right) = -\dfrac{3\pi^2 M k_{m,stress}\left(\dfrac{p_m}{Z_m} - \dfrac{p_{CF}}{Z_{CF}}\right)}{L_m^2 RT\varphi_{m,stress}\mu\left(\dfrac{1}{Z_m}\cdot\dfrac{\partial Z_m}{\partial p_m} - \dfrac{1}{p_m} + \dfrac{1}{T} + \dfrac{1}{Z_m}\cdot\dfrac{\partial Z_m}{\partial T}\right)} \\ \varphi_{m0} + \alpha_m^*\left[(\varepsilon_v - \varepsilon_{v0}) + \dfrac{(p_m - p_{m0})}{K_m} - (\varepsilon_s - \varepsilon_{s0}) - \alpha_T(T - T_0)\right] \\ k_{m,stress} = k_{m0}\left\{1 + \dfrac{\alpha_m^*}{\varphi_{m0}}\left[(\varepsilon_v - \varepsilon_{v0}) + \dfrac{(p_m - p_{m0})}{K_m} - (\varepsilon_s - \varepsilon_{s0}) - \alpha_T(T - T_0)\right]\right\}^3 \end{cases} \tag{26}$$

3.3. Gas transport in the continuous fractures

The main differences between the coal matrix and continuous fractures (CF) in the mathematical model include the following: (1) there occur two CF domains (CF-SRD and CF-NSRD) with different properties, and these two domains are connected by pressure and flow rate continuities; (2) adsorbed gas storage is not considered in the CF. The governing equation according to the mass conservation law for gas transport in the CF can be written as:

$$\frac{\partial\left(\rho_{gCF}^j\varphi_{CF,stress}^j\right)}{\partial t} + \nabla\cdot\left(-\rho_{gCF}^j\frac{k_{CF,stress}^j}{\mu}\nabla p_{CF}^j\right) = Q_{m-CF}^j \tag{27}$$

where superscript j is the domain indicator, with j = NSRD or SRD, ρ_{gCF} is the methane density in the CF, $\varphi_{CF,stress}$ is the stress-dependent CF porosity, $k_{CF,stress}$ is the stress-dependent permeability of the CF, and $Q_{m\text{-}CF}$ is the source term (from the coal matrix to the CF). Based on the previous studies of Liu et al. (1999, 2010) and Qu et al. (2012), the following equations are employed to determine $\varphi_{CF,stress}$ and $k_{CF,stress}$, respectively:

$$\varphi_{CF,stress} = \varphi_{CF0} + 3\alpha^*_{CF}(1-R_m)\left[(\varepsilon_v-\varepsilon_{v0}) + \frac{(p_{CF}-p_{CF0})}{K_m} - (\varepsilon_s-\varepsilon_{s0}) - \alpha_T(T-T_0)\right] \tag{28}$$

$$k_{CF,stress} = k_{CF0}\left\{1 + \frac{3\alpha^*_{CF}(1-R_m)}{\varphi_{CF0}}\left[(\varepsilon_v-\varepsilon_{v0}) + \frac{(p_{CF}-p_{CF0})}{K_m} - (\varepsilon_s-\varepsilon_{s0}) - \alpha_T(T-T_0)\right]\right\}^3 \tag{29}$$

where φ_{CF0} is the initial porosity of the CF, p_{CF0} is the initial gas pressure in the CF, k_{CF0} is the initial permeability of the CF, and $R_m = E/E_m$ is Young's modulus ratio of the bulk coal to the matrix. Here, R_m is very important because this parameter essentially represents the contrast between the mechanical deformation responses of the coal matrix and CF. This contrast reflects the dual-porosity features of the coalbed.

At the boundary between the SRD and NSRD, the CF gas pressure should be continuous (Li et al., 2020b):

$$p^{NSRD}_{CF}|_{SRD\ \ boundary} = p^{SRD}_{CF}|_{SRD\ \ boundary} \tag{30}$$

Moreover, the mass flux is continuous at this boundary:

$$\vec{u}^{NSRD}_{CF}|_{SRD\ \ boundary} = \vec{u}^{SRD}_{CF}|_{SRD\ \ boundary} \tag{31}$$

where $\vec{u}_{CF}$ is the mass flux of gas in the CF.

Similarly, the gas pressure and mass flux in the CF should also be continuous in the PF, which is considered an outlet boundary of gas in CF-SRD:

$$p^{SRD}_{CF}|_{PF} = p_{PF}|_{PF} \tag{32}$$

$$\vec{u}^{SRD}_{CF}|_{PF} = \vec{u}_{PF}|_{PF} \tag{33}$$

where p_{PF} is the gas pressure in the PF, and $\vec{u}_{PF}$ denotes the inflowing mass flux from CF-SRD to the PF. Combining Eqs. (25) and (27)–(33) yields the overall governing equation for the CF:

$$\begin{cases} \dfrac{\partial\left(\rho^j_{gCF}\varphi^j_{CF,stress}\right)}{\partial t} + \nabla\cdot\left(-\rho^j_{gCF}\dfrac{k^j_{CF,stress}}{\mu}\nabla p^j_{CF}\right) = \dfrac{3\pi^2 M k_{m,stress}\left(\dfrac{p_m}{Z_m}-\dfrac{p_{CF}}{Z_{CF}}\right)}{L_m^2 RT\varphi_{m,stress}\mu\left(\dfrac{1}{Z_m}\cdot\dfrac{\partial Z_m}{\partial p_m}-\dfrac{1}{p_m}+\dfrac{1}{T}+\dfrac{1}{Z_m}\cdot\dfrac{\partial Z_m}{\partial T}\right)} \\ \varphi_{CF,stress} = \varphi_{CF0} + 3\alpha^*_{CF}(1-R_m)\left[(\varepsilon_v-\varepsilon_{v0}) + \dfrac{(p_{CF}-p_{CF0})}{K_m} - (\varepsilon_s-\varepsilon_{s0}) - \alpha_T(T-T_0)\right] \\ k_{CF,stress} = k_{CF0}\left\{1 + \dfrac{3\alpha^*_{CF}(1-R_m)}{\varphi_{CF0}}\left[(\varepsilon_v-\varepsilon_{v0}) + \dfrac{(p_{CF}-p_{CF0})}{K_m} - (\varepsilon_s-\varepsilon_{s0}) - \alpha_T(T-T_0)\right]\right\}^3 \\ p^{NSRD}_{CF}|_{SRD\ \ boundary} = p^{SRD}_{CF}|_{SRD\ \ boundary};\ \ \vec{u}^{NSRD}_{CF}|_{SRD\ \ boundary} = \vec{u}^{SRD}_{CF}|_{SRD\ \ boundary} \\ p^{SRD}_{CF}|_{PF} = p_{PF}|_{PF};\ \ \vec{u}^{SRD}_{CF}|_{PF} = \vec{u}_{PF}|_{PF} \end{cases} \tag{34}$$

3.4. Gas transport in the primary fracture

In this work, the radial primary fracture (PF) is simplified as a 1-D fractured medium. Moreover, this fracture is considered the outlet boundary of CF-SRD bridging the producing well and coal mass. This modelling method has successfully captured primary fractures in stimulated shale reservoirs in previous studies (Cao et al., 2016a, 2016b; Li et al., 2020b). In particular, Li et al. (2020b) proposed a model to calculate the porosity and permeability of this type of 1-D fractured medium influenced by the varying stress with increasing gas depletion. Via the application of Li et al.'s model, we can obtain the following governing equation for the PF in the CBM reservoir:

$$\begin{cases} \dfrac{\partial(\rho_{gPF}\varphi_{PF,stress})}{\partial t} + \nabla_T\cdot\left[-b_{PF0}\rho_{gPF}\exp[C_{PF}(p_{PF}-p_{PF0})]\dfrac{k_{PF,stress}}{\mu}\nabla p_{PF}\right] = 0 \\ \varphi_{PF,stress} = \varphi_{PF0}\exp[C_{PF}(p_{PF}-p_{PF0})] \\ b_{PF,stress} = b_{PF0}\exp[C_{PF}(p_{PF}-p_{PF0})] \\ k_{PF,stress} = k_{PF0}\exp[2C_{PF}(p_{PF}-p_{PF0})] \\ p^{SRD}_{CF}|_{PF} = p_{PF}|_{PF};\ \ \vec{u}^{SRD}_{CF}|_{PF} = \vec{u}_{PF}|_{PF} \end{cases} \tag{35}$$

where ∇_T denotes the gradient operator restricted to the tangential plane of the PF, ρ_{gPF} denotes the methane density in the PF, b_{PF0}, φ_{PF0}, and k_{PF0} are the initial aperture, porosity, and permeability of the PF, respectively, and $b_{PF,stress}$, $\varphi_{PF,stress}$, and $k_{PF,stress}$ are the dynamic aperture, porosity, and permeability of the PF, respectively, influenced by stress. C_{PF} is the pore compressibility of the PF defined as $C_{PF} = \alpha_{PF}/(\varphi_{PF0}\cdot K_{PF})$. A_{PF} is the Biot coefficient of the PF, while K_{PF} is the bulk modulus of the PF. Note that the inflow of the PF is exactly provided by the outflow from CF-SRD due to the continuity of the gas flow process. Therefore, there exists no mass source term on the right-hand side of the first equation of Eq. (35).

3.5. Heat transfer

When gas is extracted from a given CBM reservoir, heat transfer

occurs due to energy change resulting from the thermal strain, heat desorption, heat convection, and heat conduction. Based on the local thermal equilibrium assumption (i.e., at one spatial point, the temperatures in the coal matrix and CF are considered approximately identical, and the thermal properties of the bulk coal are weight-averaged values based on the volumetric fractions of these two media), the energy balance can be expressed as follows (Zhu et al., 2011; Li et al., 2016; Fan et al., 2018; Dunne et al., 1996; Deng et al., 2019):

$$\frac{\partial\left[\left(\rho C_p\right)_{eff}T\right]}{\partial t}+\eta\nabla T-\nabla\cdot\left(\lambda_{eff}\nabla T\right)+K\alpha_T T\frac{\partial\varepsilon_v}{\partial t}+q_d\frac{\rho_s\rho_a}{M}\cdot\frac{\partial V_{ads}}{\partial t}=0 \tag{36}$$

where the first term on the left-hand side represents the change in internal energy, the second term is the thermal convection term, the third term is the thermal conduction term, the fourth term is the strain energy change term, and the fifth term denotes the methane sorption heat. $(\rho C_p)_{eff}$ is the effective specific heat capacity, η is the heat convection coefficient of methane, λ_{eff} is the effective thermal conductivity, and q_d is the sorption differential heat of the gas-coal system.

In the energy balance equation Eq. (36), $(\rho C_p)_{eff}$ is an average value based on the specific heat capacity and density of all the components in the coal block (Li et al., 2016; Fan et al., 2019):

$$\left(\rho C_p\right)_{eff}=(1-\gamma_{CF}\varphi_{CF}-\gamma_m\varphi_m)\rho_s C_s+\left(\gamma_{CF}\varphi_{CF}\rho_{gCF}+\gamma_m\varphi_m\rho_{gm}\right)C_g \tag{37}$$

where the first term on the right-hand side denotes the contribution of the coal skeleton to the specific heat capacity, while the second term is the contribution of gas to the specific heat capacity. C_s and C_g are the specific heat capacities of the coal grains and methane, respectively.

In the energy balance equation [Eq. (36)], η is related to the total mass flux and C_g is defined as:

$$\eta=C_g\left[\gamma_{CF}\nabla\cdot\left(-\rho^j_{gCF}\frac{k^j_{CF,stress}}{\mu}\nabla p^j_{CF}\right)+\gamma_m\nabla\cdot\left(-\frac{Mp_m k_{m,stress}}{Z_m RT\mu}\nabla p_m\right)\right] \tag{38}$$

λ_{eff} is a linear combination of the thermal conductivities of the coal skeleton and gas:

$$\lambda_{eff}=(1-\gamma_{CF}\varphi_{CF}-\gamma_m\varphi_m)\lambda_s+(\gamma_{CF}\varphi_{CF}+\gamma_m\varphi_m)\lambda_g \tag{39}$$

where λ_s and λ_g are the thermal conductivities of the coal grains and methane, respectively.

In addition, q_d in the energy balance equation [Eq. (36)] can be determined with the following equation (Dunne et al., 1996; Deng et al., 2019):

$$q_d=q_{st}-Z_{bulk}RT \tag{40}$$

where q_{st} is the isosteric sorption heat of the gas-coal system and Z_{bulk} is the bulk gas deviation factor, which can be expressed as a weighted average value of the gas deviation factors for the coal matrix (Z_m) and continuous fractures (Z_{CF}):

$$Z_{bulk}=\gamma_m Z_m+\gamma_{CF}Z_{CF} \tag{41}$$

It should be mentioned that previous studies [e.g., Li et al. (2016) and Fan et al. (2019)] have considered q_{st} instead of q_d in the energy balance equation [Eq. (36)], which actually ignores the sorption heat variation with the temperature [the term $-Z_{bulk}RT$ in Eq. (40)]. Consequently, these models could cause slight overestimations of the sorption heat. Therefore, our model includes a correction in the heat transfer computation process.

In addition, the temperature and heat flux (q_{heat}) should be continuous at the SRD boundary and PF:

$$T^{NRSD}|_{SRD\ \ boundary}=T^{SRD}|_{SRD\ \ boundary} \tag{42}$$

$$q^{NSRD}_{heat}|_{SRD\ \ boundary}=q^{SRD}_{heat}|_{SRD\ \ boundary} \tag{43}$$

$$T^{SRD}|_{PF}=T^{PF}|_{PF} \tag{44}$$

$$q^{SRD}_{heat}|_{PF}=q^{PF}_{heat}|_{PF} \tag{45}$$

Combining Eqs. (36) and (42)–(45) yields the final governing equation for heat transfer:

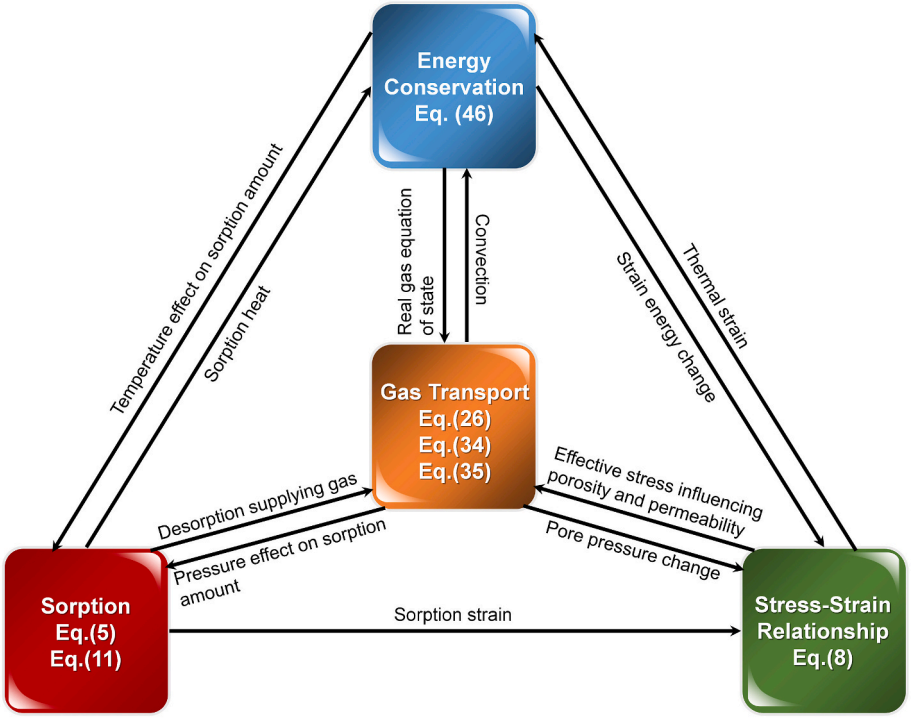

Fig. 3. Interactions between the different physical processes, including gas transport, coal deformation, non-isothermal sorption, and heat transfer.

Table 1
Comparison of the key features of previous models and the proposed model. Note: The tick mark indicates that the corresponding process/effect is considered in the model, while the cross mark indicates that the corresponding process/effect is ignored in the considered model.

Model	Reservoir	Considered key features				
		Dual-permeability rock body	Multidomain effects	Rock deformation	Heat transfer and thermal effects	Water effect
Zhu et al. (2011)	CBM reservoir	×	×	✓	✓	×
Chen et al. (2013)	CBM reservoir	✓	×	✓	×	×
Li et al. (2016)	CBM reservoir	×	×	✓	✓	✓
Li et al. (2020b)	Shale gas reservoir	✓	✓	✓	×	×
Proposed model	CBM reservoir	✓	✓	✓	✓	×

$$\begin{cases} \dfrac{\partial\left[\left(\rho C_p\right)_{eff}T\right]}{\partial t}+\eta\nabla T-\nabla\cdot\left(\lambda_{eff}\nabla T\right)+K\alpha_T T\dfrac{\partial\varepsilon_v}{\partial t}+q_d\dfrac{\rho_s\rho_a}{M}\cdot\dfrac{\partial V_{ads}}{\partial t}=0 \\ T^{NSRD}|_{SRD\ \ boundary}=T^{SRD}|_{SRD\ \ boundary};\ \ q^{NSRD}_{heat}|_{SRD\ \ boundary}=q^{SRD}_{heat}|_{SRD\ \ boundary} \\ T^{SRD}|_{PF}=T^{PF}|_{PF};\ \ q^{SRD}_{heat}|_{PF}=q^{PF}_{heat}|_{PF} \end{cases} \tag{46}$$

3.6. Coupling relationship between the different physical processes

Eqs. ((8), (26), (34), (35) and (46) construct the fully coupled, multidomain, and multiphysics model describing heat and mass transfer in the stimulated CBM reservoir. The interactions between the different physical processes are summarized in Fig. 3. With the use of this set of PDEs, gas transport, coal deformation, non-isothermal sorption, and heat transfer occurring during CBM extraction can be simulated.

The main advantage of the proposed model is that it comprehensively incorporates the above complex multiple physical processes (including gas flow, coal deformation, gas desorption, and heat transfer) into a single CBM model considering stimulation patterns. In particular, multiple thermal effects (including thermal shrinkage, non-isothermal sorption, and non-isothermal gas density change) are integrated into the combination of the different domains (including the PF, SRD, and NSRD). To highlight its innovations, the proposed model is compared to four previous unconventional gas reservoir models published by Zhu et al. (2011), Chen et al. (2013), Li et al. (2016), and Li et al. (2020b), respectively. The key features of these models are listed in Table 1. The table reveals that (1) the common feature of these five models is that they all consider fully coupled rock (coal or shale) deformation during gas extraction. (2) The model proposed by Zhu et al. (2011) is a coupled THM model based on a single-porosity-single-permeability framework. This model cannot describe the mass exchange process between the coal matrix and CF. The effects of the stark difference between matrix and CF properties on gas extraction are not reflected. In addition, Zhu et al.'s model does not consider multidomain effects, so the differences among the SRD, NSRD, and PF cannot be described. (3) The model proposed by Chen et al. (2013) is based on a dual-porosity-dual-permeability framework to describe the coal heterogeneity, but this model does not consider multidomain and thermal effects. For instance, this model neither provides specific individual equations for gas flow in the PF nor provides expressions capturing thermal strain and non-isothermal sorption. Consequently, the simulation results obtained with this model deviate from field data to a certain degree, and the impacts of different stimulation patterns cannot be simulated. (4) A notable advantage of the model proposed by Li et al. (2016) is that this model considers the water effect on CBM extraction (i.e., gas-water two-phase flow). This model is a coupled THM model. However, this model is based on a single-porosity-single-permeability framework, so the coal heterogeneity cannot be suitably described. This model also does not consider multidomain effects. (5) The model proposed by Li et al. (2020b) has been employed for shale gas reservoirs. This model comprehensively considers gas flow and deformation in multiple domains based on a dual-porosity-dual-permeability framework. Nevertheless, the heat transfer process and resultant thermal effects are not incorporated in this model. (6) The model proposed in this work not only considers coupled THM processes but also considers multidomain effects in a dual-porosity-dual-permeability framework. The proposed model can be regarded as an extension of the model of Li et al. (2016) and additionally incorporates multidomain effects. The proposed model can also be considered an extension of the model of Li et al. (2020b) by adding the consideration of thermal effects. Therefore, the proposed model combines most of the features of the other four models. The only feature ignored by the proposed model is the water effect on CBM extraction. Nevertheless, this effect has often been observed during the early period of gas extraction but slightly affects long-term CBM production, which will be examined in Section 4.1. As for the application scope, the proposed model extends the reservoir type by applying multidomain and multiphysics models originating from shale gas reservoirs to CBM reservoirs. In the model of Li et al. (2020b), a shale block was defined as a dual-porosity medium including kerogen and an inorganic matrix. Analogously, coal was defined as another dual-porosity medium, including the coal matrix and CF, in the proposed model. The definitions of these two models are similar, but the basic parameters, such as the volumetric fractions, initial porosities, initial permeabilities, adsorption capacities, and Young's moduli of coal and shale, are quite different. For instance, as an individual continuum, the CF exhibits a low Young's modulus and accounts for a small volumetric fraction of the CBM reservoir, while these two properties of the inorganic matrix (the counterpart of the CF in CBM reservoirs) are much more notable in shale reservoirs. Additionally, the slip effect of gas flow is significant in shale, but this effect can be ignored in CBM reservoirs due to the larger cleat aperture than that of the fissures encountered in shale reservoirs (Chen et al., 2013; Li et al., 2020b). Another difference between shale and CBM reservoirs is that the stimulation patterns are more varied than those in stimulated shale reservoirs because more stimulation approaches, such as blasting, are typically applied in CBM reservoirs (Zhu et al., 2012; Cao et al., 2017a; Zhang et al., 2018). We will further examine the performance of different stimulation patterns in CBM extraction in Section 5.1.1 (below). In summary, the proposed model incorporates sufficient advantages based on previous studies and extends previous models to achieve a fine description of CBM reservoirs and accurate CBM extraction simulation.

4. Model verification

To verify and apply the proposed multidomain and multiphysics model, two CBM extraction cases were simulated with the established model based on information reported in the literature. The simulation results were compared to field data and results obtained with several previously published CBM reservoir models to demonstrate the validity and reliability of the proposed model.

4.1. Simulation case 1: CBM extraction in the southern Qinshui Basin, China

The gas extraction process in a CBM reservoir with a vertical well in the southern Qinshui Basin in Shanxi Province, China, was simulated with the proposed model. The computed results of the daily gas production were matched to a set of production data stemming from field

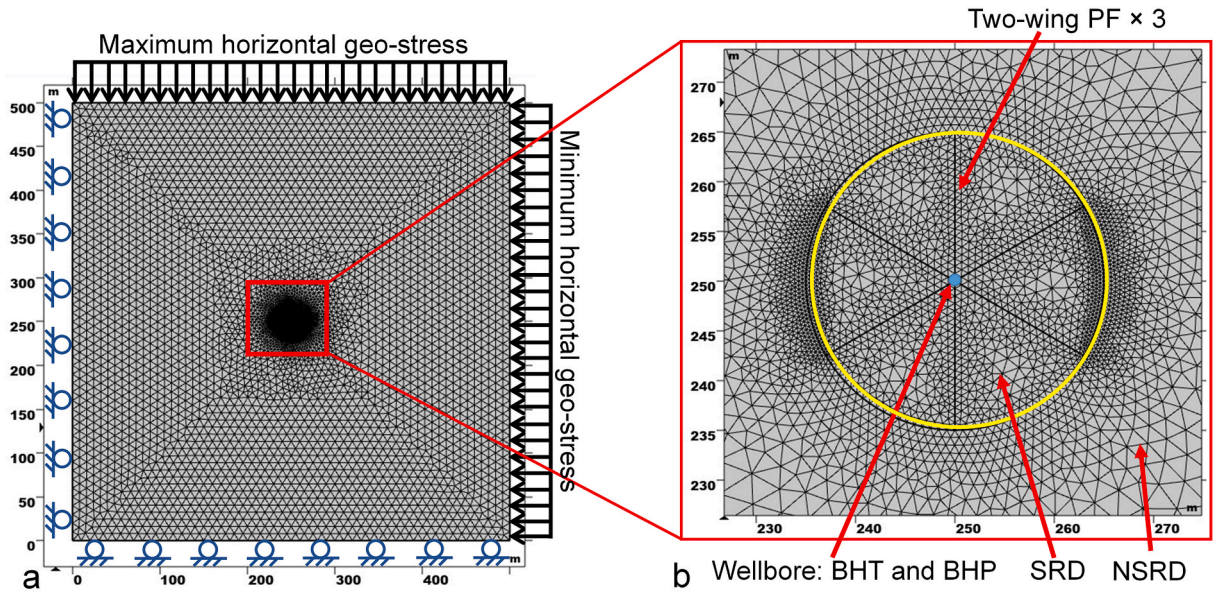

Fig. 4. Mesh geometry and boundary conditions of **Simulation Case 1** (CBM extraction in the southern Qinshui Basin) with the proposed model: (a) Top view of the meshed geometry of the stimulated CBM reservoir with the in situ boundary conditions. (b) Zoomed-in image of the central area, showing the producing well, PFs, SRD, and part of the NSRD.

observations. The field data and most of the parameters were collected from the work published by Li et al. (2016). However, certain important parameters (such as the bottom-hole pressure) were not given in the original reference. Another issue was that the model proposed by Li et al. (2016) is based on a single-porosity-single-permeability framework, while our model is based on a dual-porosity-dual-permeability framework. Therefore, some of the undetermined parameters were set according to another previous study describing a dual-porosity-dual-permeability model developed by Chen et al. (2013). Other missing coal properties were collected from Wu et al. (2010b) and Xia et al. (2014). The fully coupled PDEs derived in Section 3 were numerically solved in COMSOL Multiphysics (Version 5.4), a commercial PDE solver based on the finite element method. As shown in Fig. 4(a), a 2-D geometry with 13,188 mesh elements was built to represent the CBM reservoir for numerical simulation purposes. Regarding the boundary conditions, the CBM reservoir was subject to a geo-stress field orthogonally decomposed as the maximum horizontal geo-stress and the minimum horizontal geo-stress, while roller constraints were defined along the left and bottom boundaries. These settings reflect the influence of the in situ geo-stress field on coal deformation and have been applied in previous studies on unconventional gas reservoir simulation (Cao et al., 2016a; Li et al., 2016, 2020b). A zoomed-in image of the central area of the reservoir is shown in Fig. 4 (b). A producing well with a certain bottom-hole temperature (BHT = 293.5 K), a constant bottom-hole pressure (BHP = 1.0 MPa), and wellbore radius of 0.11 m, is located at the centre of the square CBM reservoir (500 m × 500 m × 5 m). Three double-wing PFs were explicitly specified and symmetrically distributed around the vertical wellbore. The half-PF length is 15 m, and the angle between each pair of PFs is 60°. These PFs are totally included within a circular SRD with a radius of 15 m. In contrast, the CF and coal matrix are simulated via the dual-continuum modelling method, which generates coupled results computed based on the proposed PDEs at each node (Li et al., 2020b). A detailed simulation parameter list is given in Table 2, in which CF-SRD and CF-NSRD exhibit different initial porosities, initial permeabilities, and mechanical properties (including Young's modulus, Poisson's ratio, and Biot coefficient). In addition, to measure the simulation accuracy, average relative errors (δ_{ave}s) of the simulated daily production curves obtained with the various models were calculated based on the following equation (assuming that the field data are the true values):

$$\delta_{ave} = \frac{1}{n}\sum_{i=1}^{n}\frac{P_{d,sim,i} - P_{d,field,i}}{P_{d,field,i}} \tag{47}$$

where n is the total number of data points, $P_{d,sim,i}$ is the daily gas production simulated with the model at data point i, and $P_{d,field,i}$ is the simulated daily gas production with the model at data point i. A smaller absolute value of δ_{ave} indicates a higher simulation accuracy.

The simulated daily gas production curve (the red curve) obtained with the proposed model was compared to the field data (the scattered dots), as shown in Fig. 5. Overall, a great consistency was realized, indicating a satisfactory accuracy (δ_{ave} = 2.24%) of the proposed model for CBM extraction. Note that the simulation results at the very beginning are higher than the field data to a certain degree because the proposed model ignores the blockage effect of water in the reservoir on gas flow during this period. This drawback will be improved in our future work. Nevertheless, the water effect usually diminishes with increasing gas depletion and is not significant from the perspective of long-term unconventional gas extraction, which has been demonstrated in previous studies [e.g., Sakhaee-Pour and Bryant (2012) and Jurus et al. (2013)]. To compare the performance levels of the different models, the simulation results obtained with the coupled THM model proposed by Li et al. (2016) are also shown in Fig. 5 (the blue curve, δ_{ave} = 2.69%). Both the proposed model and Li et al.'s model exhibited a great performance in data matching. More specifically, Li et al.'s model better matched the early-stage (during the first 60 days) production data than our model did because the former model considers the effect of water (gas-water two-phase flow) on CBM extraction, while our model ignores this effect. However, our model performed better in matching the data after 800 days of gas extraction because our model is based on a dual-porosity-dual-permeability framework instead of Li et al.'s model, which is based on a single-porosity-single-permeability framework. The dual-permeability model distinguishes the coal matrix and coal cleats to better describe gas flow in the coal matrix, which is dominant during the middle and late periods of CBM extraction. As a result, dual-permeability models usually achieve more accurate predictions of long-term CBM production than those achieved by single-permeability models (Chen et al., 2013).

Table 2
Reservoir properties and computational parameters of **Simulation Case 1** (CBM extraction in the southern Qinshui Basin) for model verification (Zhang et al., 2008; Chen et al., 2013; Xia et al., 2014; Li et al., 2016).

Parameter (unit)	Value	Parameter (unit)	Value
Reservoir dimensions (m × m × m)	500 × 500 × 5	Wellbore radius (m)	0.11
Half-PF length (m)	15	SRD radius (m)	15
Minimum horizontal geo-stress (Pa)	4.51×10^6	Maximum horizontal geo-stress (Pa)	4.916×10^6
Angle between adjacent PFs (°)	60	Initial reservoir temperature (K)	312.5
Initial reservoir pressure (Pa)	5.24×10^6	Bottom-hole pressure (Pa)	1.38×10^6
Bottom-hole temperature (K)	293.5	Methane viscosity (Pa•s)	1.84×10^{-5}
Coal density (kg/m^3)	1470	Langmuir strain constant	0.06
Langmuir pressure (Pa)	5.67×10^6	Langmuir volume (m^3/kg)	5.5×10^{-3}
Specific heat capacity of coal grains [J/(kg•K)]	1350	Specific heat capacity of methane [J/(kg•K)]	2160
Reference temperature for desorption testing (K)	300	Thermal conductivity of coal grains [W/(m•K)]	0.197
Convection thermal conductivity of methane [W/(m•K)]	0.031	Thermal expansion coefficient of coal (K^{-1})	2.4×10^{-5}
Pressure correction coefficient for the sorption curve (Pa^{-1})	7×10^{-8}	Temperature correction coefficient for the sorption curve (K^{-1})	0.02
Isosteric heat of adsorption (J/mol)	33,400	Specific heat capacity ratio	1.32
Bulk modulus of the matrix (Pa)	5.04×10^9	Young's modulus of the matrix (Pa)	8.47×10^9
Matrix size (m)	4.0	Initial matrix porosity	0.045
Volumetric fraction of the CF	0.04	Biot coefficient of the matrix	0.25
Initial matrix permeability (m^2)	1.0×10^{-17}	Initial PF porosity	0.2
Initial PF permeability (m^2)	6.0×10^{-14}	Initial PF aperture (m)	0.003
Pore compressibility of the PF (Pa^{-1})	1×10^{-9}	Molar weight of methane (kg/mol)	0.016
Young's modulus of the CF (Pa)	SRD: 1.2×10^8 NSRD:4.0×10^9	Young's modulus ratio	SRD: 0.32 NSRD: 0.53
Poisson's ratio of the CF	SRD: 0.39 NSRD: 0.36	Initial CF porosity	SRD: 0.12 NSRD: 0.08
Initial CF permeability (m^2)	SRD: 6.0×10^{-15} NSRD:3.0×10^{-16}	Biot coefficient of the CF	SRD: 0.9 NSRD: 0.5

4.2. Simulation case 2: CBM extraction in the Fruitland Coal, United States

To further verify the performance and flexibility of the proposed model, gas extraction in a CBM reservoir with a single vertical, gas-phase well in the Fruitland Coal, San Juan Basin, United States, was simulated with the proposed model. This case was investigated in a previous study (Chen et al., 2013). Therefore, the main parameters and conditions were set according to this previous paper. As shown in Fig. 6, a 2-D geometry with 4932 mesh elements was built to represent the CBM reservoir for numerical simulation purposes. Note that neither the SRD nor the PF exists in this geometry. Thus, this case could be regarded as the scenario (an unstimulated CBM reservoir with only one producing well) shown in Fig. 1(b), which is a degeneration of the base scenario depicted in Fig. 1(a). Regarding the boundary conditions, the square CBM reservoir was surrounded by fixed restrictions according to Chen et al. (2013), as shown in Fig. 6(a). Furthermore, the input bottom-hole pressure was based on a curve (the black curve, $\delta_{ave} = 4.97\%$) fitted to the field data (the scattered green squares), as shown in Fig. 6(b). The computing parameters and reservoir properties considered in this case were mainly collected from Chen et al. (2013). Certain missing reservoir parameters were obtained from Zhang et al. (2008) and Xia et al. (2014). The parameters related to thermal effects were based on Zhu et al. (2011) and Li et al. (2016). All the parameters/properties are listed in Table 3. Daily gas production data measured in the field (scattered dots) and the simulation results of the proposed model (red curve) are shown in Fig. 7. A notable consistency ($\delta_{ave} = -1.45\%$) between the simulation results and field data could be observed, demonstrating the high reliability of our model in simulations. In addition, the simulation results obtained with two numerical models previously proposed by Chen et al. (2013) for the same case are shown in Fig. 7 for comparison. The blue curve indicates the results of the single-permeability model ($\delta_{ave} = 11.71\%$), while the dark golden curve denotes the results of the dual-permeability model ($\delta_{ave} = 4.75\%$). Fig. 7 shows that both previous models obtained significantly larger average relative errors than those obtained with our model. The results of the single-permeability model established by Chen et al. (2013) exhibited significant deviation from the field data during the period from 100 to 1600 days. Although the matching performance of the dual-permeability model developed by Chen et al. (2013) was better than that of the single-permeability model due to the incorporation of the mass exchange process between the coal matrix and CF, moderate deviations in the simulation results from the field data could still be observed during the period from 600 to 2000 days. In contrast, our model performed well throughout the whole simulation period because it not only considers dual-permeability features but also considers thermal effects. In summary, **Simulation case 1** confirmed the reliability of our model in simulating a CBM reservoir with SRD, NSRD, and PF domains, while **Simulation case 2** demonstrated that our model performs satisfactorily in simulating an unstimulated CBM reservoir with only the NSRD and one producing well. Comprehensive incorporation of multidomain effects, dual-porosity-dual-permeability features, and multiple physical processes ensured the high simulation accuracy and flexibility of our model in managing CBM reservoirs regardless of whether these reservoirs are stimulated or unstimulated.

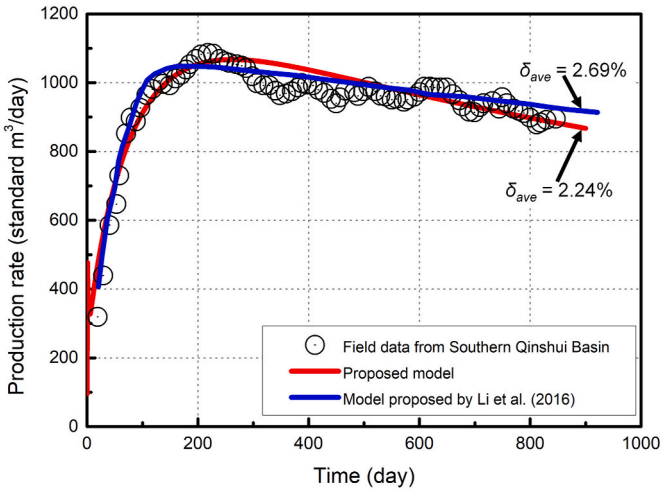

Fig. 5. Comparison of the simulation results of the daily CBM production obtained with the proposed model and the model of Li et al. (2016) and the field data in **Simulation Case 1** (CBM extraction in southern Qinshui Basin).

5. Results and discussion

The proposed fully coupled model is a tool for the evaluation of CBM production and provides a deep understanding of this process since this model comprehensively includes various characteristics, mechanisms,

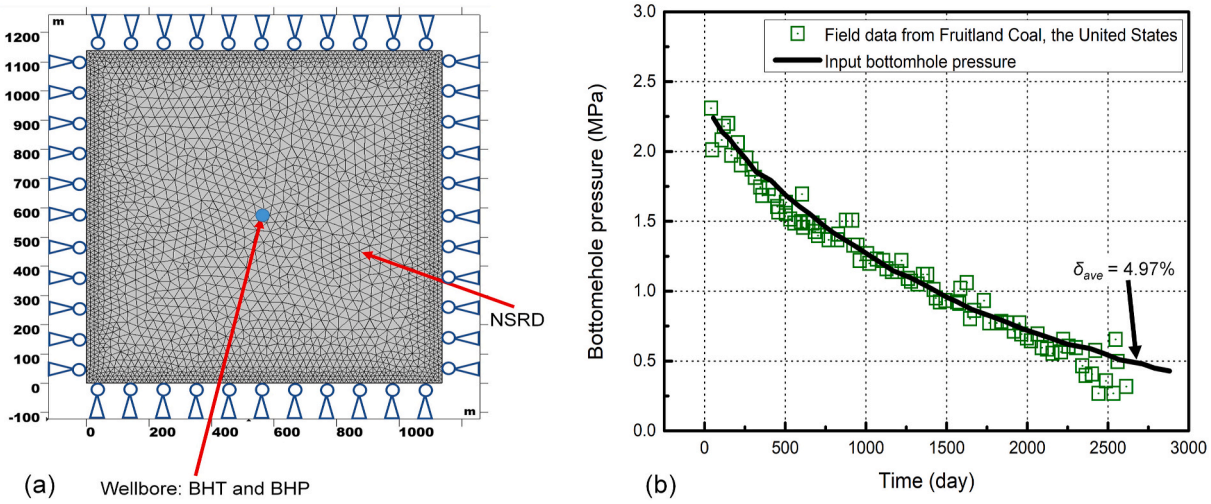

Fig. 6. Geometry and boundary conditions of **Simulation Case 2** (CBM extraction in the Fruitland Coal, United States): (a) meshed geometry (top view) and mechanical boundary conditions. (b) Bottom-hole pressure data measured in the field (Chen et al., 2013) and the input bottom-hole pressure based on a fitting curve.

Table 3
Reservoir properties and computational parameters of **Simulation Case 2** (CBM extraction in the Fruitland Coal, United States) for model verification (Zhang et al., 2008; Zhu et al., 2011; Chen et al., 2013; Xia et al., 2014; Li et al., 2016).

Parameter (unit)	Value	Parameter (unit)	Value
Reservoir dimensions (m × m × m)	1137.98 × 1137.98 × 14	Wellbore radius (m)	0.108
Initial reservoir pressure (Pa)	3.447×10^6	Initial reservoir temperature (K)	312.5
Bottom-hole temperature (K)	293.5	Bottom-hole pressure (Pa)	1.38×10^6
Coal density (kg/m^3)	1300	Methane viscosity (Pa•s)	1.228×10^{-5}
Langmuir pressure (Pa)	5.67×10^6	Langmuir strain constant	0.02
Specific heat capacity of the coal grains [J/(kg•K)]	1350	Langmuir volume (m^3/kg)	4.2×10^{-3}
Reference temperature for desorption testing (K)	300	Specific heat capacity of methane [J/(kg•K)]	2160
Convection thermal conductivity of methane [W/(m•K)]	0.031	Thermal conductivity of the coal grains [W/(m•K)]	0.197
Pressure correction coefficient for the sorption curve (Pa^{-1})	7×10^{-8}	Thermal expansion coefficient of coal (K^{-1})	2.4×10^{-5}
Isosteric heat of adsorption (J/mol)	33,400	Temperature correction coefficient for the sorption curve (K^{-1})	0.02
Bulk modulus of matrix (Pa)	2.13×10^{10}	Specific heat capacity ratio	1.32
Matrix size (m)	5.5	Young's modulus of the matrix (Pa)	3.59×10^{10}
Volumetric fraction of the CF	0.05	Initial matrix porosity	0.044
Initial matrix permeability (m^2)	3.0×10^{-18}	Biot coefficient of the matrix	0.2
Young's modulus of the CF (Pa)	9.37×10^7	Molar weight of methane (kg/mol)	0.016
Poisson's ratio of the CF	0.36	Young's modulus ratio	0.1
Initial CF permeability (m^2)	3.0×10^{-14}	Initial CF porosity	0.02
Biot coefficient of the CF	0.5		

and interactions between the different media and domains in CBM reservoirs. In this section, two issues, namely, multidomain and thermal effects, are examined based on the simulation results obtained with the proposed model to gain insights into the heat and mass transfer

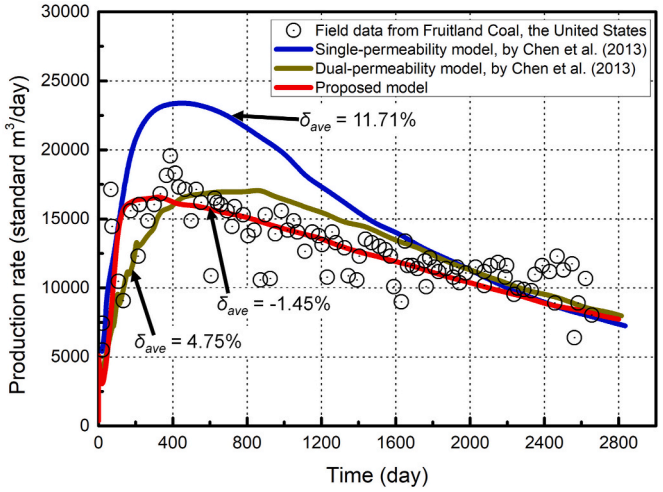

Fig. 7. Comparison of the simulation results of the daily CBM production obtained with the proposed model, the single-permeability model of Chen et al. (2013), the dual-permeability model of Chen et al. (2013), and the field data for **Simulation Case 2** (CBM extraction in the Fruitland Coal, United States).

processes during CBM extraction. The former issue is closely related to the evaluation of the effects of stimulation treatments (such as hydraulic fracturing) on CBM production, while the latter is often ignored in previous studies on CBM extraction. The results described in this section are based on a sensitivity analysis of a typical simulation case (referred to as the base case), which was adapted from **Simulation Case 1** (Southern Qinshui Basin Coalbed), as mentioned in Section 4.

5.1. *Influence of the multidomain effects on CBM extraction*

5.1.1. *Effects of the stimulation pattern on gas production*

The reservoir and computational parameters of the base case are listed in Table 4. Compared to the parameters of **Simulation Case 1** listed in Table 2, the differences in the initial permeabilities between the PF, CF, and coal matrix in the base case were increased to highlight the importance of multiscale characterization. The properties of coal grains related to thermal effects were also modified to study these effects. In addition, the PF length, SRD radius, and reservoir size were adjusted. To investigate the effects of the stimulation pattern on gas production, the five scenarios introduced in Fig. 1 [i.e., (1) unstimulated coalbed; (2) 1

Table 4
Reservoir properties and computational parameters in the base case.

Parameter (unit)	Value	Parameter (unit)	Value
Reservoir dimension (m × m × m)	200 × 200 × 5	Wellbore radius (m)	0.11
Half-PF length (m)	40	SRD radius (m)	40
Minimum horizontal geo-stress (MPa)	4.51	Maximum horizontal geo-stress (MPa)	4.916
Angle between adjacent PFs (°)	60	Initial reservoir temperature (K)	343.15
Initial reservoir pressure (Pa)	5.24	Bottom-hole pressure (Pa)	1.38×10^6
Bottom-hole temperature (K)	303.15	Methane viscosity (Pa•s)	1.84×10^{-5}
Coal density (kg/m^3)	1470	Langmuir strain constant	0.02
Langmuir pressure (Pa)	5.67×10^6	Langmuir volume (m^3/kg)	4.2×10^{-3}
Specific heat capacity of the coal grains [J/(kg•K)]	1350	Specific heat capacity of methane [J/(kg•K)]	2160
Reference temperature for desorption testing (K)	300	Thermal conductivity of the coal grains [W/(m•K)]	0.788
Convection thermal conductivity of methane [W/(m•K)]	0.031	Thermal expansion coefficient of coal (K^{-1})	9.6×10^{-5}
Pressure correction coefficient for the sorption curve (Pa^{-1})	7×10^{-8}	Temperature correction coefficient for the sorption curve (K^{-1})	0.02
Isosteric heat of adsorption (J/mol)	33,400	Specific heat capacity ratio	1.32
Bulk modulus of the matrix (Pa)	5.04×10^9	Young's modulus of the matrix (Pa)	8.47×10^9
Matrix size (m)	2.0	Initial matrix porosity	0.045
Volumetric fraction of the CF	0.05	Biot coefficient of the matrix	0.25
Initial matrix permeability (m^2)	3.0×10^{-18}	Initial PF porosity	0.2
Initial PF permeability (m^2)	1.0×10^{-12}	Initial PF aperture (m)	0.003
Pore compressibility of the PF (Pa^{-1})	1×10^{-9}	Molar weight of methane (kg/mol)	0.016
Young's modulus of the CF (Pa)	SRD: 1.45×10^8 NSRD:4.0×10^9	Young's modulus ratio	SRD: 0.32 NSRD: 0.53
Poisson's ratio of the CF	SRD: 0.39 NSRD: 0.36	Initial CF porosity	SRD: 0.12 NSRD: 0.08
Initial CF permeability (m^2)	SRD: 3.0×10^{-16} NSRD:3.0×10^{-17}	Biot coefficient of the CF	SRD: 0.9 NSRD: 0.5

double-wing PF + NSRD; (3) 3 PFs + NSRD; (4) SRD + NSRD; and (5) 3 PFs + SRD + NSRD (i.e., base case)] were simulated with the proposed model. The cumulative production levels under these 5 scenarios during 50-year gas extraction are shown in Fig. 8(a). It could be observed that the different stimulation patterns significantly influenced CBM production. Specifically, the cumulative production curve in the base case stabilized at approximately 12,000 days, demonstrating that most of the recoverable gas had been extracted. In contrast, all of the other four scenarios exhibited lower extraction rates than those in the base case. Furthermore, adopting the 50-year cumulative production in the base case (5.06×10^5 standard m^3) as the total exploitable gas amount, the cumulative production ratio (CPR, ranging from 0% to 100%) could be defined as the current cumulative production divided by the total exploitable gas amount to measure the degree of gas extraction. Note that CPR = 0 corresponds to an unexploited reservoir, while CPR = 100% indicates a fully exploited reservoir. Thus, a series of CPR values at different time points (1, 5, 10, 25, and 50 years) under the different scenarios could be calculated, as shown in Fig. 8(b). During the early period of gas extraction (0–5 years), the CPR values under the different scenarios significantly differed, indicating the remarkably higher effectiveness of the base case pattern than that under the other 4 scenarios. For instance, after 1 year of production, the base case pattern obtained the highest CPR value (25.1%), while the CPR value of the unstimulated coalbed reached only 3.3%. The larger number of PFs benefitted gas production improvement, which was demonstrated by the difference in CPR value between the 1 double-wing PF + NSRD (10.3%) and 3 PFs + NSRD (17.7%) patterns at the 1-year time point. In addition, the CPR value under the SRD + NSRD scenario at 1 year reached 16.3%, which varied between those under the 1 PF + NSRD and 3 PFs + NSRD scenarios and was much lower than that in the base case. During the middle period of gas extraction (5–25 years), the base case continued to exhibit a high production efficiency, and almost all of the exploitable gas (CPR = 97.6%) was extracted at 25 years. In contrast, the unstimulated coalbed only obtained a CPR value of 52.3%. The other 3 stimulation patterns achieved higher efficiencies to different degrees than that obtained for the unstimulated CBM reservoir (by more than 30% at 25 years). During the late period of gas extraction (25–50 years), the increase in CPR values of the stimulated reservoirs declined because the residual exploitable gas decreased. Although the CPR value of the unstimulated CBM reservoir continued to increase during the late period, it reached only 72.9% at 50 years, indicating that a considerable fraction of the exploitable gas remained unrecovered. Obviously, the creation of both the SRD and multiple PFs greatly helped to achieve a rapid extraction process.

To better understand the gas extraction process, CF pressure evolutions under the five scenarios with the different stimulation patterns are shown in Fig. 9. Additionally, matrix pressure evolution trends under the five scenarios are shown in Fig. 10. Comparing these two figures, a difference in pressure evolution due to the different patterns and a difference in pressure evolution between the CF and coal matrix could be clearly observed. During the early and middle periods of gas extraction, there existed an apparent pressure difference between the CF and matrix under each scenario due to the much faster drainage process in the highly permeable CF than that in the tight matrix. With increasing gas depletion, this pressure difference dwindled and eventually became very small. These results reflect the typical behaviour of a dual-porosity-dual-permeability system and represent the gas flow sequence illustrated in Fig. 2(b). An interesting issue is the difference in production behaviour between the 3 PFs + NSRD and SRD + NSRD patterns. Fig. 8 shows that the 3 PFs + NSRD pattern led to faster gas recovery during the early period, but the recovery process gradually fell behind that under the SRD + NSRD pattern during the middle and late periods and yielded a lower CPR than that under the SRD + NSRD scenario after 50 years of extraction. The various effects of the SRD and multiple PFs on improving gas production during the different periods could be attributed to the distinct heterogeneities caused by these two stimulation components. Generally, the PF permeability exhibited an enormous contrast with the original reservoir permeability (i.e., much more permeable than the NSRD), which caused a very high pressure gradient near the PFs as the driving force of the gas flow. In contrast, the SRD exhibited a relatively moderate permeability contrast with the NSRD, while it exhibited a much larger area than that of the PF. Therefore, the main advantage of the PF was to achieve a high pressure gradient within a narrow zone, while the merit of the SRD was to create a moderate pressure gradient in a large area. In the 3 PFs + NSRD case, the high pressure gradient caused by the PFs resulted in fast recovery during the early period of gas production. Moreover, this stimulation pattern generated a significant heterogeneity in the pressure distribution in the SRD. This heterogeneity indicated that there always remained residual exploitable gas in the reservoir throughout the whole extraction process. In contrast, in the SRD + NSRD case, most of the exploitable gas in the SRD was smoothly extracted during the early/middle period because of the notable homogeneity of the SRD. This suggests that the residual gas in the SRD could be effectively extracted, which helped to realize a high ultimate recovery. These results indicate that a suitable stimulation pattern

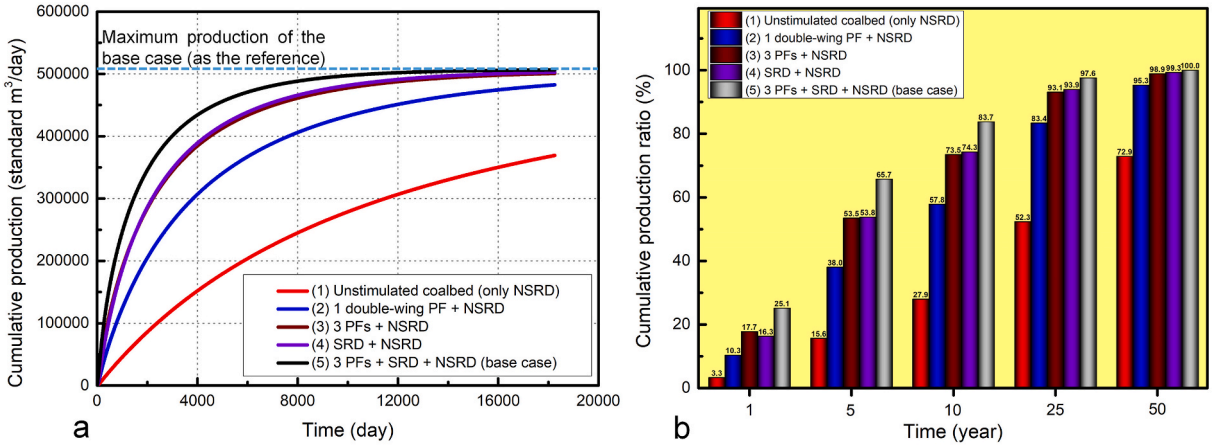

Fig. 8. Effects of the stimulation pattern on the 50-year CBM production. (a) Cumulative production of the CBM reservoirs with the different stimulation patterns. (b) Cumulative production ratios (CPRs) of the CBM reservoirs with the different stimulation patterns, adopting the 50-year cumulative production in the base case [5.06×10^5 standard m^3, corresponding to the blue dashed line in Fig. 8(a)] as the reference. (For interpretation of the references to colour in this figure legend, the reader is referred to the Web version of this article.)

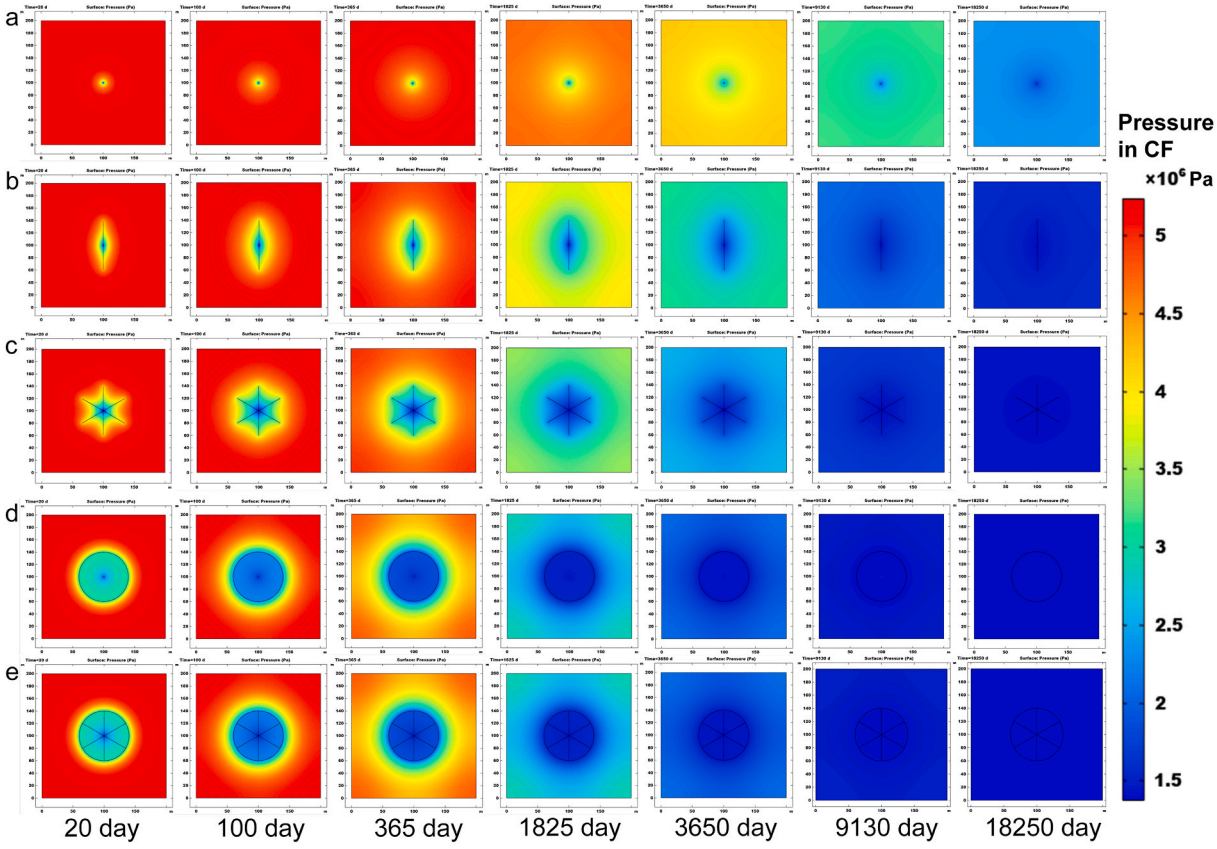

Fig. 9. CF pressure evolution under the scenarios with the different stimulation patterns. (a) Unstimulated coalbed; (b) 1 double-wing PF + NSRD; (c) 3 PFs + NSRD; (d) SRD + NSRD; and (e) 3 PFs + SRD + NSRD (base case).

should be designed according to the engineering objective so that corresponding stimulation techniques can be selected. In engineering practice, if the main objective of CBM extraction is to obtain gas as rapidly as possible during a limited period (as required in many cases of natural gas exploitation), the creation of multiple PFs with extremely high permeability is the key target of stimulation (e.g., via hydraulic fracturing). If the main objective of CBM extraction is to ensure that the gas content within a large area decreases to the required low level and/or greatly enhance the ultimate recovery (as required by gas pre-extraction operations to ensure mining safety), the establishment of a relatively homogeneous SRD with numerous micro-fractures is the key goal of stimulation [e.g., via certain types of deep-hole blasting techniques, as reported by Zhang et al. (2018)]. Surely, if a specific stimulation treatment could form a combination of both multiple PFs and a large SRD, as shown in the base case [e.g., CO_2 fracturing; refer to the details in Cao et al. (2017a)], the merits of these two stimulation patterns could be fulfilled simultaneously, and CBM could be extracted both quickly and thoroughly (similar to the base case). In summary,

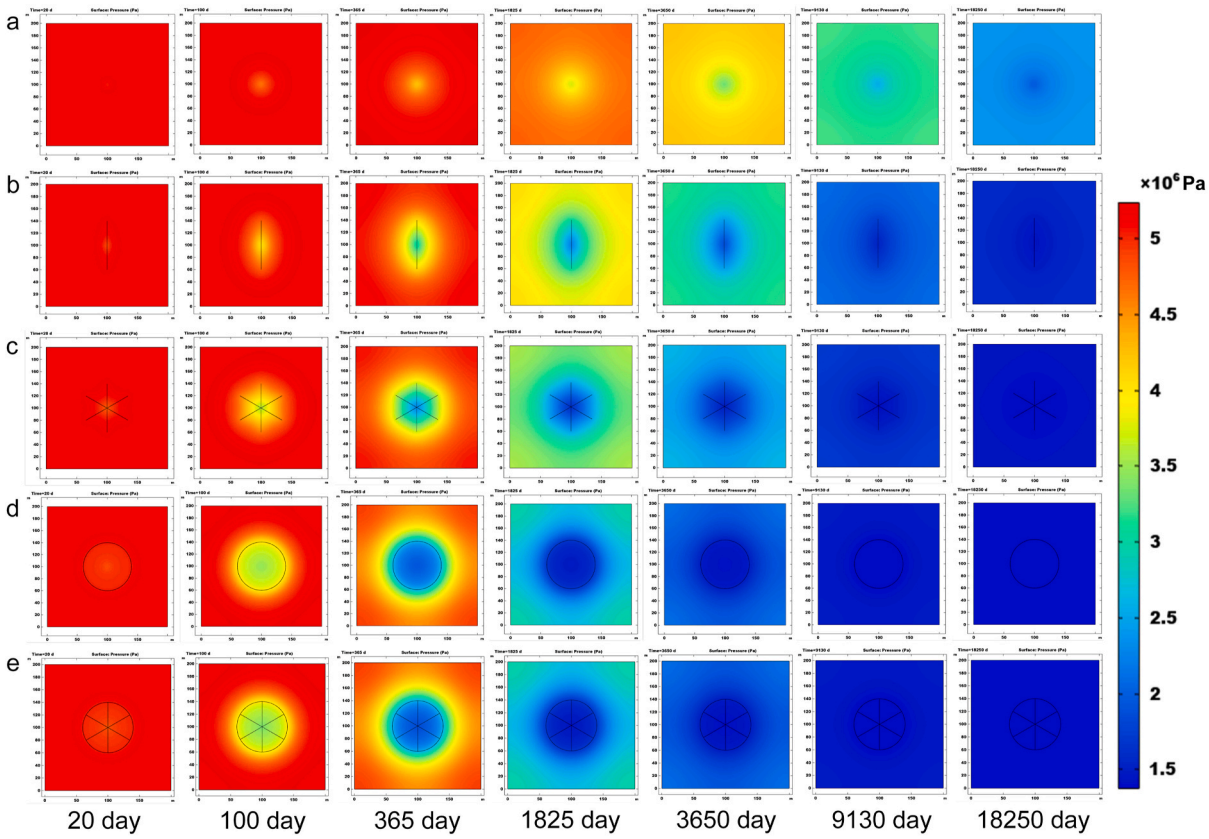

Fig. 10. Matrix pressure evolution under the scenarios with the different stimulation patterns. (a) Unstimulated coalbed; (b) 1 double-wing PF + NSRD; (c) 3 PFs + NSRD; (d) SRD + NSRD; and (e) 3 PFs + SRD + NSRD (base case).

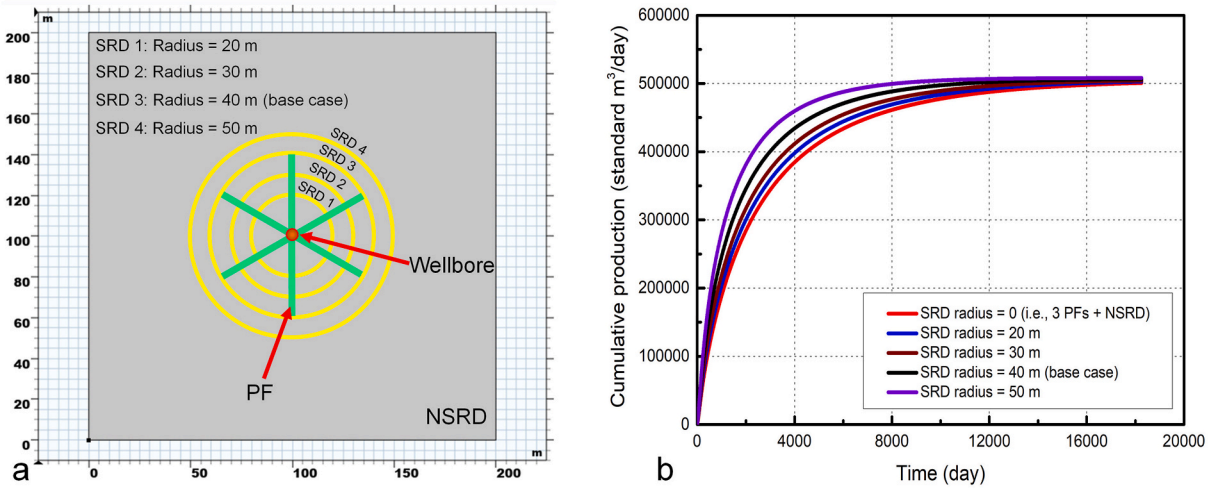

Fig. 11. Effects of the SRD size on CBM extraction. (a) Illustration of CBM reservoirs containing 3 PFs and SRDs of different radii, including 20 m, 30 m, 40 m, and 50 m; (b) effects of the SRD radius on the cumulative production during the 50-year gas extraction period.

enhancing the complexity of fracture patterns as much as possible through stimulations is the key to CBM extraction improvement. The remainder of this paper examines the gas extraction process considering the base case.

5.1.2. *Effects of the SRD properties on CBM production*

5.1.2.1. Effects of the SRD size on CBM production. Regarding the gas extraction process in a stimulated CBM reservoir, the actual SRD radius does not necessarily match the PF half-length (similar to the base case) but may be larger or smaller. This is related to coal fracture/fragment mechanisms, which depend on the type and effectiveness of the stimulation technique applied (Zhu et al., 2012; Liu et al., 2018; Zhang et al., 2018, 2020b; Gao et al., 2019; Li et al., 2020b). As illustrated in Fig. 11 (a), gas extraction in CBM reservoirs with SRDs of different radii, including 20 m, 30 m, 40 m (base case), and 50 m, were simulated with the proposed model. The obtained cumulative production amounts under these scenarios, along with that in the 3 PFs + NSRD case (i.e., SRD radius = 0), are shown in Fig. 11(b) to reveal the effects of the SRD size on gas production. Enlarging the SRD radius significantly helped

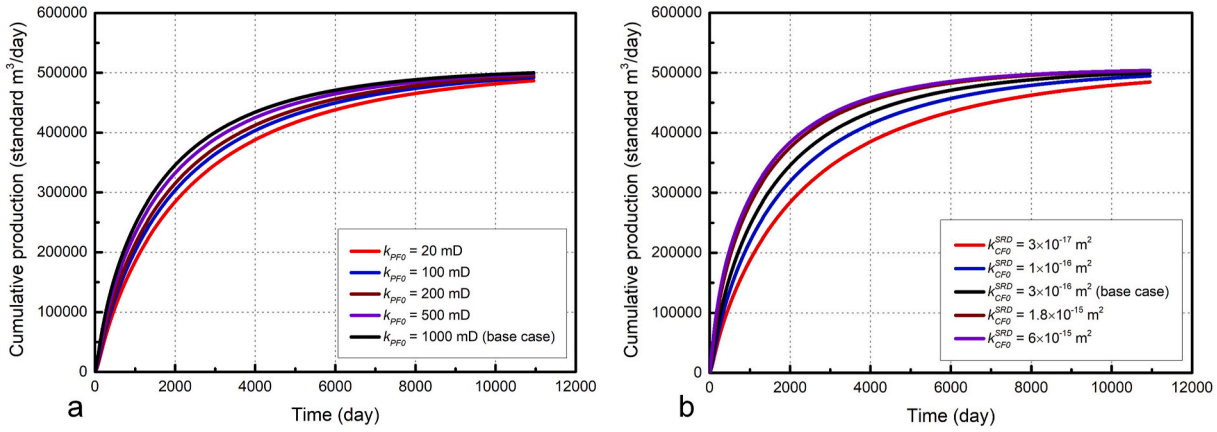

Fig. 12. Effects of the initial PF and CF-SRD permeabilities on CBM extraction. (a) Effects of the PF permeability on the cumulative gas production; (b) effects of the CF-SRD permeability on the cumulative gas production.

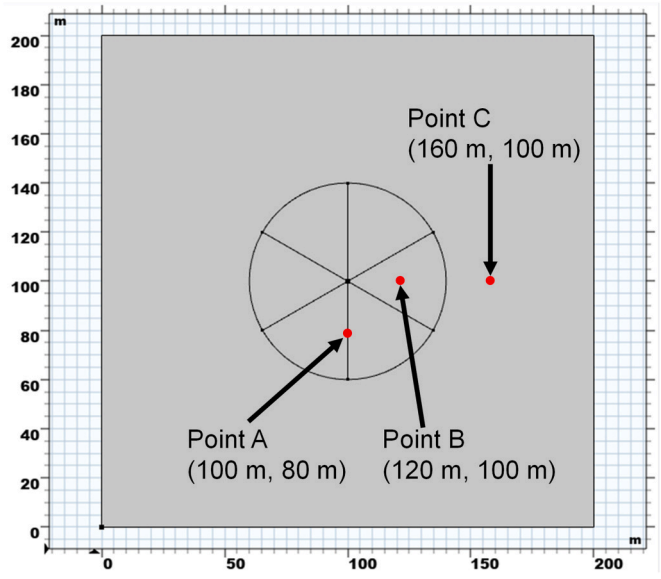

Fig. 13. Points representing the different domains in a stimulated CBM reservoir. Point A represents the PF; Point B indicates the SRD; Point C denotes the NSRD.

improve the gas recovery during the early and middle periods of production. For example, after 1 year of gas extraction, the cumulative production in the case with an SRD radius = 20 m was 11.9% higher than that in the case without an SRD, while the cumulative production in the case with an SRD radius = 50 m achieved a 51.6% enhancement over that in the case without an SRD. At the 10-year time point, the cumulative production in the case with an SRD radius = 20 m was 3.8% higher than that in the case without the SRD, while the cumulative production in the case with an SRD = 50 m realized a 21.3% enhancement. These results highlight the importance of creating an as large as possible SRD to improve CBM production. The remainder of this paper continues to examine the CBM extraction process considering the base case in 30 years of production. The reason why 30 years is adopted as the investigated production time span of the simulations is that most of the exploitable gas in the base case could be produced during this period [CPR = 98.7%, as shown in Fig. 11(a)].

5.1.2.2. Effects of the initial PF and SRD permeabilities on CBM production. As mentioned above, stimulation treatment could create PFs and SRD with an enhanced porosity and permeability, while the original properties of the NSRD are not modified. Therefore, the effects of the initial PF permeability (k_{PF0}) and CF-SRD permeability (k^{SRD}_{CF0}) on the cumulative production during a 30-year extraction period were studied. Note that the effects of the enhanced porosities of the PF and SRD were not studied here because these quantities are mainly reflected by the corresponding permeability enhancement. As shown in Fig. 12(a), a higher initial PF permeability promoted rapid gas recovery. For instance, the cumulative production of the reservoir with $k_{PF0} = 1 \times 10^{-12}$ m^2 (1000 mD) after 5 years of extraction was 23.0% higher than that of the reservoir with $k_{PF0} = 2 \times 10^{-14}$ m^2 (20 mD). Similarly, Fig. 12 (b) shows that improving the initial permeability of CF-SRD significantly enhanced the speed of gas extraction. For example, the cumulative production of the reservoir with $k^{SRD}_{CF0} = 6 \times 10^{-15}$ m^2 (6 mD) after 5 years of extraction was 37.8% higher than that of the reservoir with $k^{SRD}_{CF0} = 3 \times 10^{-17}$ m^2 (0.03 mD). Fig. 12 also shows that the enhancement effect of either k_{PF0} or k^{SRD}_{CF0} on gas production experienced an upper limit. For example, if $k^{SRD}_{CF0} > 1.8 \times 10^{-15}$ m^2, the production improvement with increasing k^{SRD}_{CF0} was negligible. Therefore, compared to techniques that can only generate either PFs or an SRD, stimulation techniques creating both PF and SRD (e.g., CO_2 fracturing) could achieve faster CBM extraction by increasing the complexity of fractures.

5.1.3. Effects of the mechanical coupling relationship on CBM production

In CBM extraction, the mechanical coupling relationship is a key influencing factor. This relationship reflects the effects of effective stress on the coal porosity, permeability, and resultant gas production. In a stimulated CBM reservoir with multiple domains, the mechanical coupling effects are particularly complicated because these different domains with distinct mechanical properties yield varied mechanical responses (i.e., deformations) during gas depletion. In this subsection, the effects of the PF and CF-SRD compressibilities on the 30-year CBM extraction level were studied. Not only the cumulative production but also the stress-dependent permeabilities of PF ($k_{PF,stress}$), CF-SRD ($k^{SRD}_{CF,stress}$), and CF-NSRD ($k^{NSRD}_{CF,stress}$) were studied. The investigated points representing the PF, SRD, and NSRD of the model geometry are shown in Fig. 13. The cumulative production amounts of the reservoirs with different PF compressibilities are shown in Fig. 14(a). A higher PF compressibility resulted in slower CBM extraction, which could be ascribed to the more severe closure of the PF. In CBM extraction, the pressure in the PF rapidly declined, increasing the effective stress in the PF. Thus, the porosity and permeability of the PF with high compressibility significantly decreased, hindering CBM extraction. Conversely, if the PF exhibited low compressibility, the permeability loss induced by PF closure could be limited [please refer to the changing ratio of the PF ($k_{PF,stress}/k_{PF0}$) depicted in Fig. 14(b)], so the daily production decline

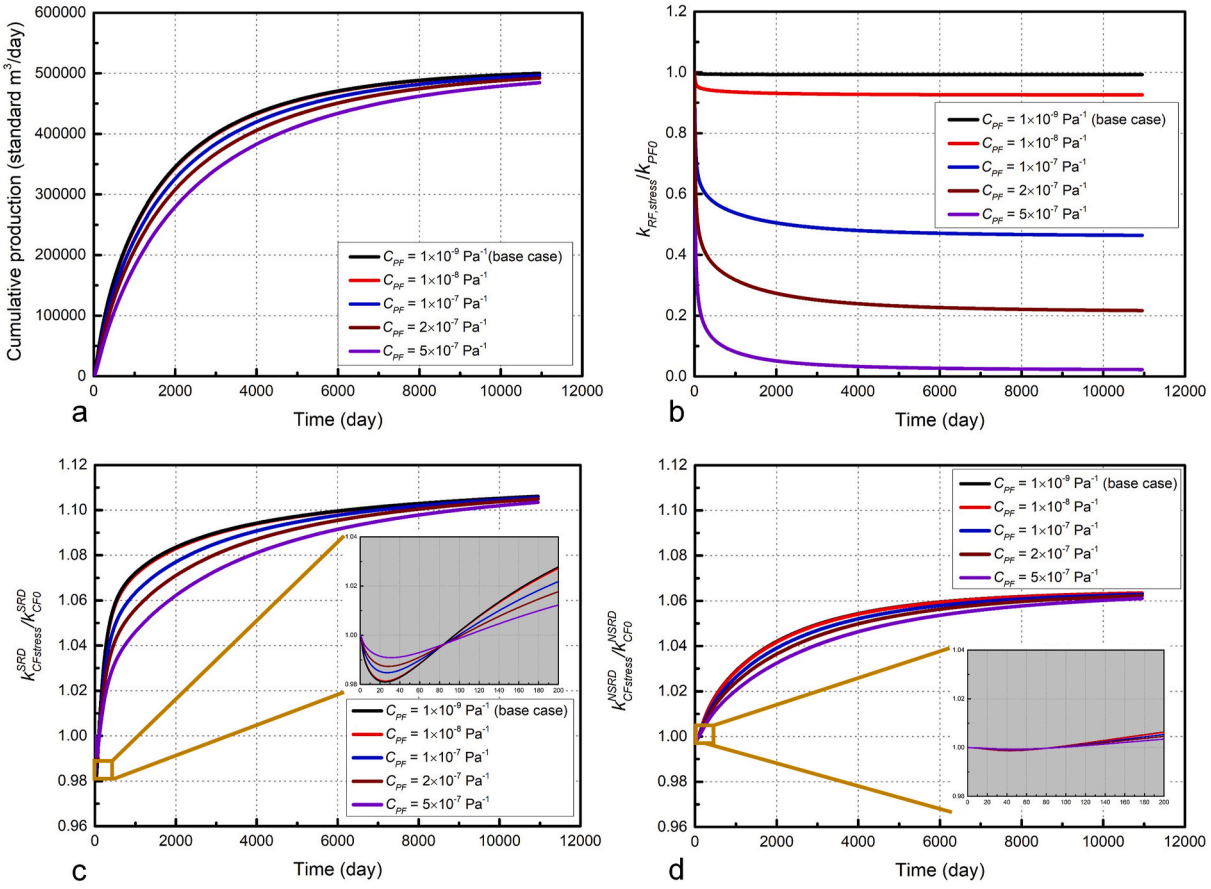

Fig. 14. Effects of the PF compressibility on the 30-year CBM extraction amount. (a) Effects of the PF compressibility on the cumulative production. (b) Effects of the PF compressibility on the PF permeability evolution. (c) Effects of the PF compressibility on the stress-dependent CF permeability in the SRD (inset: the first 200 days of extraction). (d) Effects of the PF compressibility on the stress-dependent CF permeability in the NSRD (inset: the first 200 days of extraction).

was not as great as that in the case with a high PF compressibility. In some hydraulic fracturing treatments, proppants are not applied in the stimulated fractures because the targeted coalbed tends to be too soft to uphold these materials, which is different from hydraulic fracturing operations in shale gas reservoirs in which proppants are often injected. Therefore, the negative effect of PF closure on production could be significant in CBM extraction, which should be given more attention. As shown in Fig. 14(c), the stress-dependent CF permeability in the SRD ($k^{SRD}_{CF,stress}$) first decreased and then rebounded at a certain time point. This phenomenon, shown more clearly in the inset of Fig. 14(c) ($k^{SRD}_{CF,stress}$ evolution over the first 200 days), is consistent with the theoretical calculation results and field observations reported in many previous studies on CBM extraction (Palmer and Mansoori, 1998; Shi and Durucan, 2004; Cui and Bustin, 2005; Zhang et al., 2008). Similarly, Fig. 14 (d) shows a decrease-rebound-increase evolution trend of $k^{NSRD}_{CF,stress}$, although this variation was much less notable than that in $k^{SRD}_{CF,stress}$. Moreover, a change in PF compressibility also led to different permeability evolution trends of the SRD and NSRD [as shown in Fig. 14(c) and (d), respectively]. A higher value of the PF compressibility corresponded to smaller permeability variations in the SRD and NSRD, which is the result of the complex mechanical coupling effect throughout the whole reservoir with increasing production time.

The influences of the pore compressibility of the SRD (C^{SRD}) on the 30-year CBM extraction amount were also studied. Here, C^{SRD} is a compound physical quantity defined according to the following expression based on previous studies (Palmer and Mansoori, 1998; Cui and Bustin, 2005; Li et al., 2020b):

$$C^{SRD} = \frac{\alpha^{SRD}}{\varphi_0^{SRD} K^{SRD}} \tag{48}$$

where K^{SRD} is the bulk volumetric modulus of the SRD, α^{SRD} is the bulk Biot coefficient of the SRD, and φ_0^{SRD} is the bulk initial porosity of the SRD. These quantities are averaged values of the CF and coal matrix based on the volumetric fraction (Berryman, 2002; Mehrabian and Abousleiman, 2015; Cao et al., 2016a):

$$\alpha^{SRD} = \alpha_{CF}^{SRD} + \alpha_m = \frac{\gamma_{CF} K^{SRD} \alpha_{CF}^{*SRD}}{K_{CF}^{SRD}} + \frac{\gamma_m K^{SRD} \alpha_m^*}{K_m} \tag{49}$$

$$\varphi_0^{SRD} = \gamma_{CF} \varphi_{CF0}^{SRD} + \gamma_m \varphi_{m0} \tag{50}$$

For example, C^{SRD} in the base case could be determined as 3.42×10^{-8} Pa^{-1} according to the parameters provided in Table 4. We varied the value of E_{CF}^{SRD} to obtain a series of C^{SRD} values to simulate the corresponding CBM extraction processes with our model. With the different SRD compressibility values, the cumulative production amounts are shown in Fig. 15(a), and the stress-dependent permeability evolutions of the PF, CF-SRD, and CF-NSRD during CBM extraction are shown in Fig. 15(b), (c), and (d), respectively. A higher C^{SRD} value corresponded to slower CBM extraction [as shown in Fig. 15(a)] because this resulted in greater shrinkage of the SRD [i.e., a significantly lower $k^{SRD}_{CF,stress}$ value, as shown in Fig. 15(c)]. Conversely, if C^{SRD} is very low, $k^{SRD}_{CF,stress}$ exhibits an increasing trend during gas extraction because the enhancing effects of gas desorption and thermal strains on the CF porosity and permeability prevail over the shrinkage effect. Moreover, the change in C^{SRD} resulted in different permeability evolution trends of the PF and NSRD

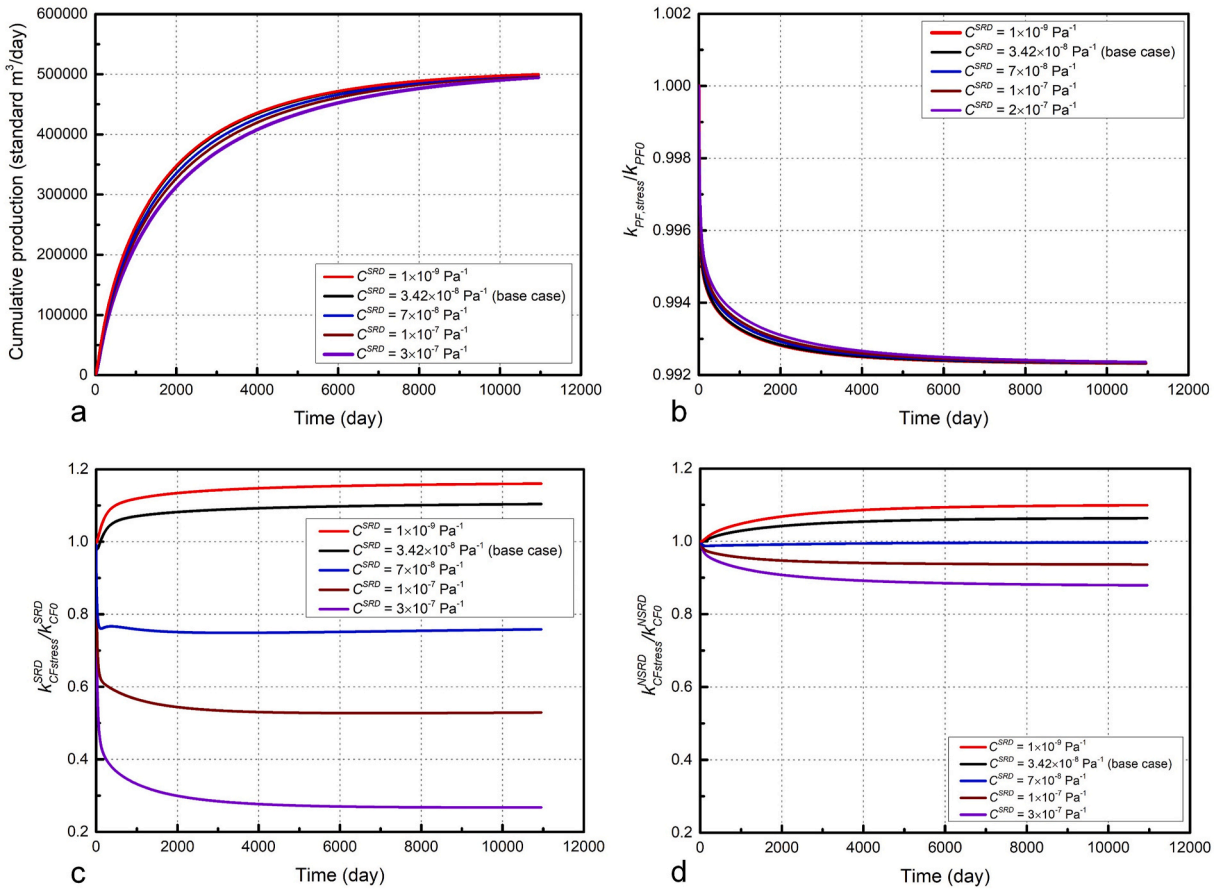

Fig. 15. Effects of the SRD compressibility on the 30-year CBM extraction amount. (a) Effects of the PF compressibility on the cumulative production. (b) Effects of the SRD compressibility on the PF permeability evolution. (c) Effects of the SRD compressibility on the stress-dependent CF permeability of the SRD. (d) Effects of the SRD compressibility on the stress-dependent CF permeability of the NSRD.

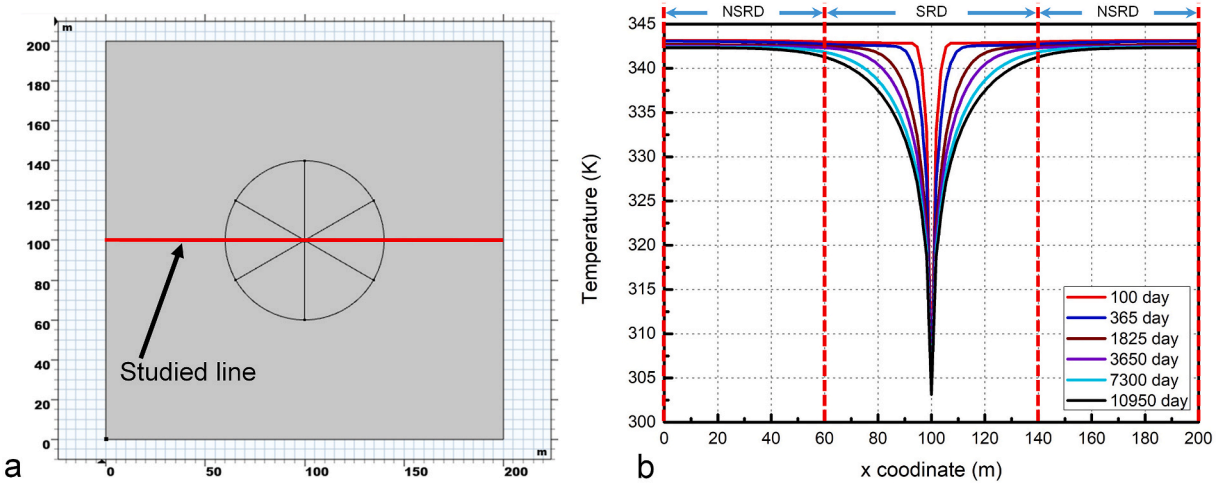

Fig. 16. Temperature distribution evolution during 30 years of CBM production. (a) The investigated line. (b) Temperature distribution evolution along the investigated line in the base case during 30 years of CBM production.

[as shown in Fig. 15(b) and (d), respectively] due to the mechanical interactions between the different domains. Specifically, a higher C^{SRD} value caused a lower permeability in the NSRD due to the intensified compression effect of the entire coalbed, while a higher C^{SRD} value slightly impeded the reduction in the PF permeability because greater shrinkage of the coal mass indicated weaker closure of the PF (Palmer and Mansoori, 1998; Shi and Durucan, 2004; Cui and Bustin, 2005; Zhang et al., 2008). In view of the various evolution trends of the different domains, differentiating the PF, SRD, and NSRD in stimulated CBM reservoir modelling and simulation is important to accurately characterize the complex changes in these domains. In some previous studies on unconventional gas extraction, the stimulated part of the reservoir was oversimplified as a set of primary hydraulic fractures without an SRD (Cao et al., 2016a, 2016b, 2017b), which may cause a

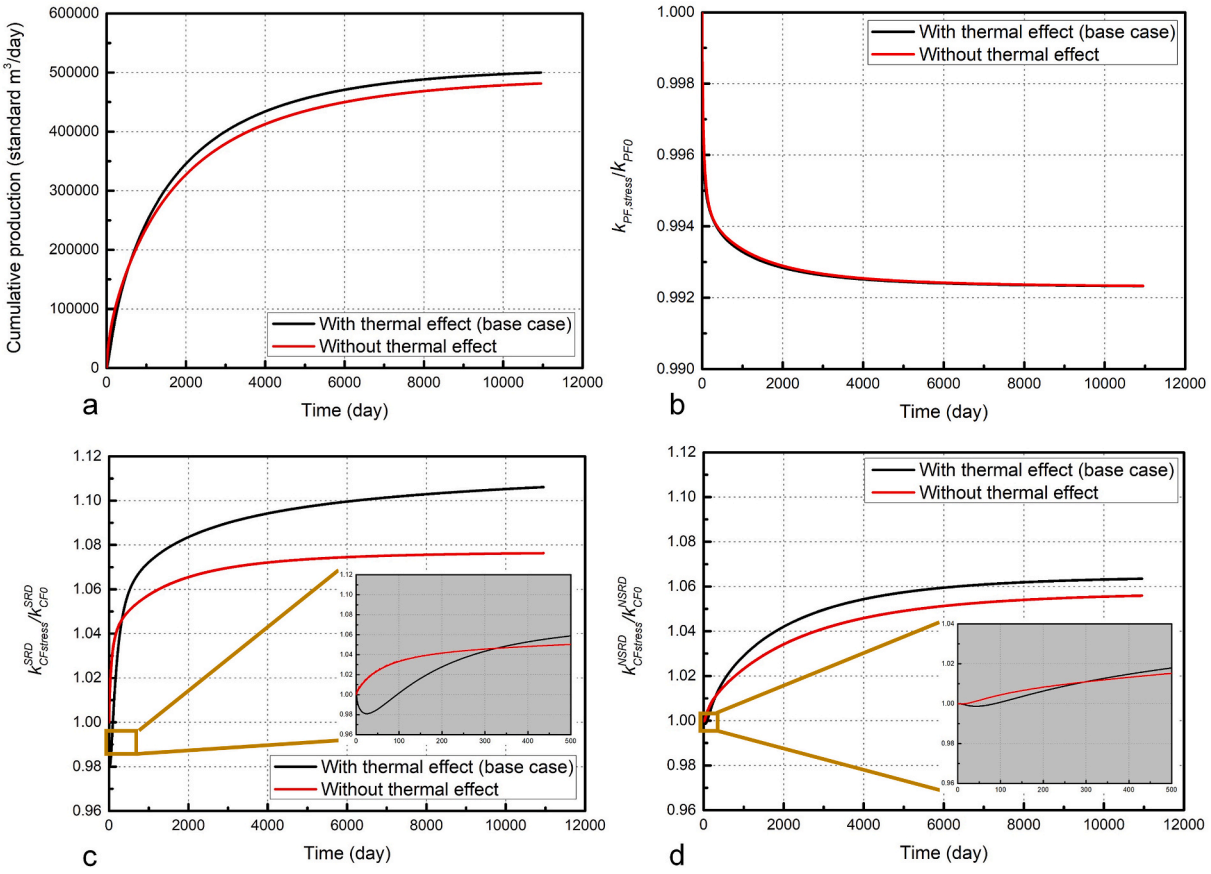

Fig. 17. Influence of the thermal effects on cumulative production and permeability. (a) Comparison of the cumulative production with/without consideration of thermal effects during 30 years of production. (b) Comparison of the stress-dependent permeability of the PF with/without consideration of thermal effects during 30 years of production. (c) Comparison of the stress-dependent permeability of the SRD with/without considering thermal effects during 30 years of production (inset: the first 500 days of extraction). (d) Comparison of the stress-dependent permeability of the NSRD with/without considering thermal effects during 30 years of production (inset: the first 200 days of extraction).

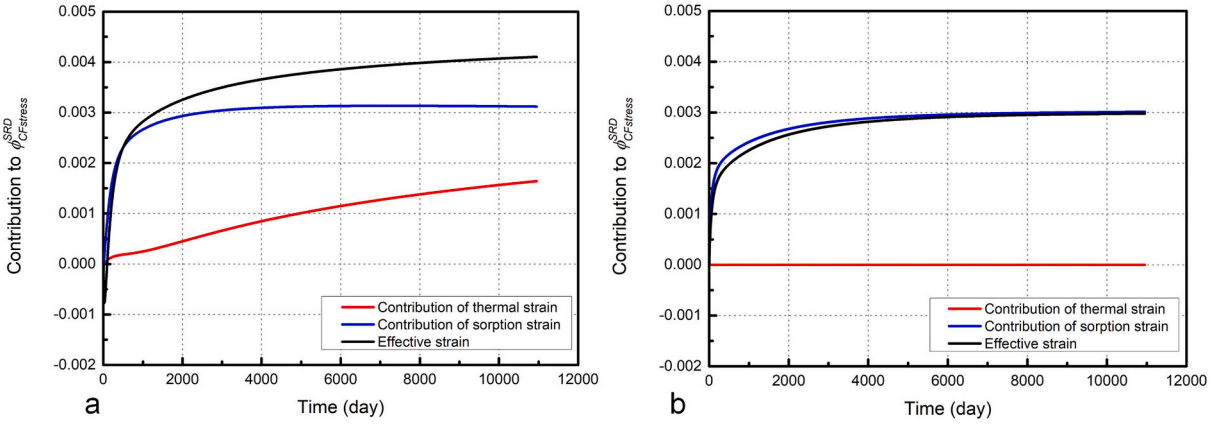

Fig. 18. Contributions of the various strains to the stress-dependent porosity of CF-SRD. (a) Considering thermal effects (the base case). (b) Without consideration of thermal effects.

certain deviation of the simulation results from the real conditions, especially in those reservoirs stimulated via blasting and/or CO_2 fracturing in which a large number of secondary fractures are generated within a large volume. In brief, the SRD plays a key role in CBM extraction. It is conducive to obtaining accurate results to treat the SRD as a separate domain (with unique properties) interacting with the other domains of the reservoir.

5.2. Influence of the thermal effects on CBM extraction

5.2.1. Temperature evolution

The evolution of the temperature distribution in the base case during 30-year gas extraction was simulated. Choosing an equator line through the reservoir as the investigated target [refer to the red line in Fig. 16 (a)], the obtained temperature distribution evolution trend along the line is shown in Fig. 16(b), revealing a wellbore-centred, low-

temperature zone gradually extending towards the deep reservoir with increasing gas depletion. As described in Eq. (36), the temperature distribution is the combined result of thermal convection, thermal conduction, strain energy change, and desorption heat. It should also be noted that the temperature drop in the SRD occurs much faster than that in the NSRD because of the greater heat transfer accompanying the faster gas flow in the SRD. These results are automatically employed to further compute the thermal effects on gas production and reservoir permeability described in the following text.

5.2.2. Thermal effects on CBM production and permeability evolution

To evaluate the thermal effects on CBM extraction, the evolutions of the cumulative production and permeability in the base case with/without consideration of thermal effects are shown in Fig. 17. Cumulative production curves during 30 years of CBM extraction are shown in Fig. 17(a). It is revealed that the cumulative production considering thermal effects is lower than that without considering thermal effects during the early period, while the opposite holds after approximately 600 days. For example, at the 100-day time point, the cumulative production considering thermal effects (3.74×10^4 standard m^3) equalled 57.7% of that without considering thermal effects (6.48×10^4 standard m^3), while after 10,950 days (30 years) of extraction, the cumulative production (5.00×10^4 standard m^3) was 3.82% higher than that without considering thermal effects (4.82×10^4 standard m^3). Furthermore, stress-dependent permeability evolution trends of the PF ($k_{PF,stress}$), CF-SRD ($k^{SRD}_{CF,stress}$), and CF-NSRD ($k^{NSRD}_{CF,stress}$) are shown in Fig. 17 (b), (c), and (d), respectively. There was a slight difference in $k_{PF,stress}$ between the results with/without thermal effects during the whole 30-year CBM extraction period. In contrast, $k^{SRD}_{CF,stress}$ and $k^{NSRD}_{CF,stress}$with thermal effects were lower than those without thermal effects during the early period, while the opposite was observed during the middle and late periods. Specifically, $k^{SRD}_{CF,stress}$ with thermal effects exceeded that without thermal effects at 325 days [refer to the inset of Fig. 17(c)], and $k^{NSRD}_{CF,stress}$ with thermal effects surpassed that without thermal effects at 300 days [refer to the inset of Fig. 17(d)]. The change in the contrast relationship between the cumulative production with and without thermal effects is closely associated with the roles of sorption-induced and thermal strains in permeability evolution during the different periods. Choosing CF-SRD as an example, the contributions of thermal strain, sorption-induced strain, and effective strain to the stress-dependent porosity ($\varphi_{CF,stress}$) in the base case are shown in Fig. 18. Comparing these curves with [refer to Fig. 18(a)] and without [refer to Fig. 18(b)] thermal effects, it could be found that during the early period of CBM production, the enhancement effect of desorption-induced-shrinkage strain on $\varphi_{CF,stress}$ was important. The desorption-induced shrinkage strain with thermal effects was lower than that without thermal effects because temperature decrease negatively affects desorption [as expressed in Eqs. (5), (6) and (11)]. This results in lower $\varphi_{CF,stress}$ and $k^{SRD}_{CF,stress}$ values with thermal effects than those without thermal effects during the early period. According to the theory of sorption science, a lower temperature suggests greater adsorption gas retention, i.e., a lower desorption gas supply and lower desorption strain (Zhu et al., 2011; Atkins et al., 2014; Li et al., 2016). For example, after 100 days, the contribution of the desorption (shrinkage) strain to the $\varphi_{CF,stress}$ change with thermal effects was 8.7×10^{-4}, which only equalled 55.1% of that without thermal effects (1.58×10^{-3}). Consequently, the cumulative production with thermal effects was lower than that without thermal effects during the early period. However, with continued gas depletion, the enhancement effect of thermal (shrinkage) strain on the porosity in Fig. 18(a) became increasingly more important and eventually constituted the crucial factor of porosity increase during the middle and late periods of production, while the contribution of the desorption (shrinkage) strain on $\varphi_{CF,stress}$ tended to stabilize during these periods. Thus, permeability enhancement with thermal effects gradually prevailed over that without thermal effects, resulting in a higher cumulative production with thermal effects than that without thermal effects at the end of the 30-year CBM extraction period. In summary, non-isothermal sorption effects and thermal strain competitively influence CBM production and reservoir permeability. Ignoring thermal effects may overestimate CBM production and permeability because of overestimation of the sorption-induced strain or underestimation of CBM production and permeability due to not considering the thermal strain.

Table 5
Coefficients used to investigate the cases with different degrees of thermal effects.

Case name	α_T (K^{-1})	λ_s [W/(m*K)]	q_{st} (J/mol)
(1) Without thermal effects	–	–	–
(2) With slight thermal effects	2.4×10^{-5}	0.197	18,500
(3) With moderate thermal effects (base case)	9.6×10^{-5}	0.788	33,400
(4) With strong thermal effects	4.8×10^{-4}	1.576	96,400

5.2.3. Influences of the coefficients related to thermal effects on CBM production

The influences of three important coefficients of the energy balance equation, including the thermal expansion coefficient (α_T), thermal conductivity of coal grains (λ_s), and isosteric sorption heat of gas (q_{st}), on CBM production were investigated for further evaluation of the thermal effects. Each CBM reservoir exhibits unique values of these three coefficients due to the variability in coal grains. Higher values of these coefficients indicate stronger thermal effects. Here, four cases describing different degrees of thermal effects were investigated, including (1) without thermal effects; (2) with slight thermal effects; (3) with moderate thermal effects (i.e., the base case); and (4) with strong thermal effects. The thermal-effect coefficients considered in these cases are listed in Table 5. The 30-year cumulative production levels and permeabilities of the different domains in the four cases are shown in Fig. 19. As shown in Fig. 19(a), during the early period of extraction, the cumulative production levels under the different degrees of thermal effects were lower than that in the case without thermal effects, while the cumulative production eventually became higher than that in the case without thermal effects during the middle and late periods. These results are consistent with the results shown in Fig. 17(a). Among the three cumulative production curves with different degrees of thermal effects, the case with the strongest thermal effects corresponded to the highest cumulative production during the early period, but this case yielded the lowest cumulative production during the late period. This could be ascribed to the competitive effects of thermal strain and non-isothermal sorption during the different periods, as discussed in Section 5.2.2. On the one hand, the stress-dependent permeabilities of the PF, CF-SRD, and CF-NSRD shown in Fig. 19(a), (b), and (c), respectively, indicate that stronger thermal shrinkage effects cause higher permeabilities in the different domains, which benefits gas production improvement. On the other hand, stronger thermal effects promote heat transfer and lead to a more notable temperature reduction throughout the reservoir [refer to the temperature evolutions of the SRD and NSRD with different degrees of thermal effects, as shown in Fig. 20(a) and **(b)**, respectively], which indicates higher adsorbed gas retention. Note that stronger thermal effects correspond to less extractable adsorbed gas, according to non-isothermal sorption theory (Zhu et al., 2011; Atkins et al., 2014; Li et al., 2016). The evolution trends of the adsorbed gas volume per unit of coal mass as the standard gas volume (V_{ads}s) computed with the non-isothermal sorption equation in the SRD and NSRD are shown in Fig. 21(a) and (b), respectively, demonstrating that stronger thermal effects hinder gas desorption to a certain degree in both the SRD and in NSRD. Again, these results reveal that the various

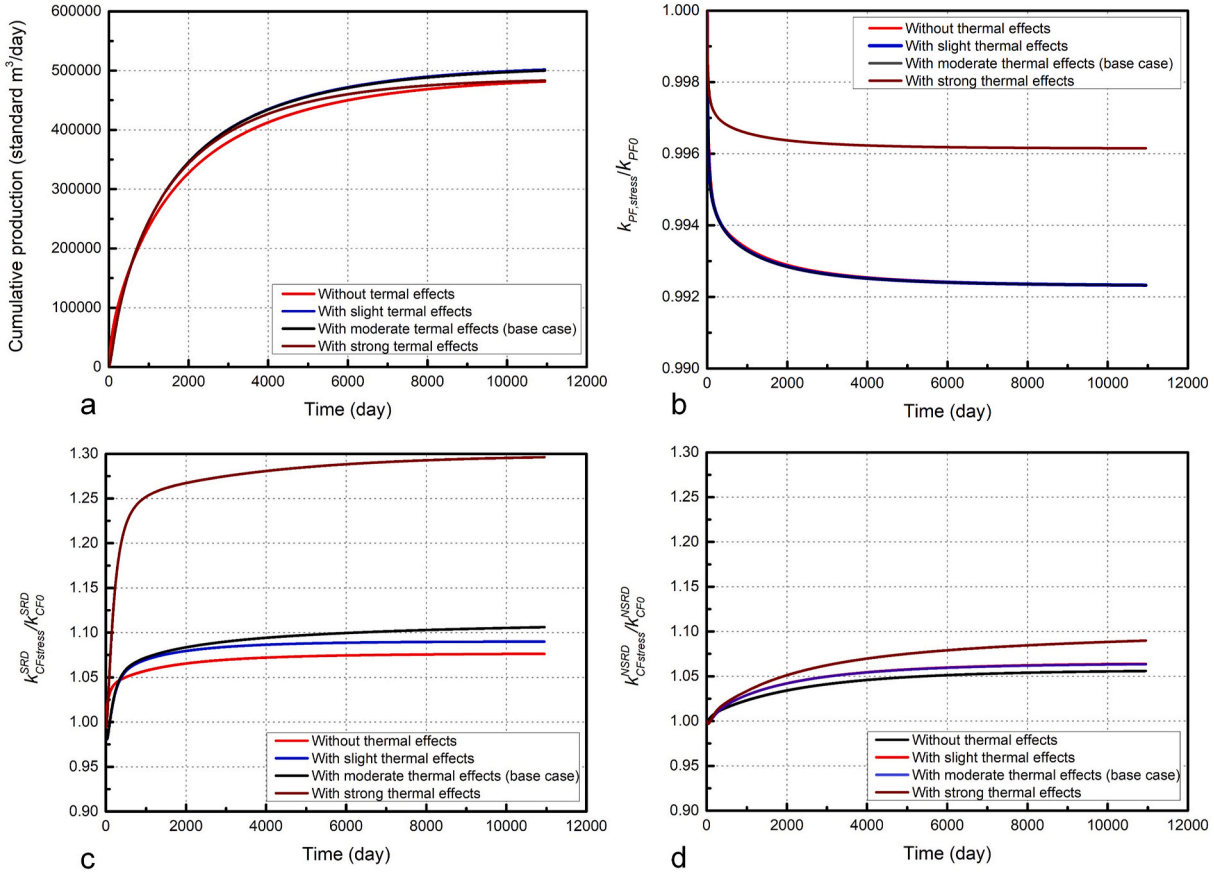

Fig. 19. Influences of the different degrees of thermal effects on the cumulative production and permeability. (a) Comparison of the cumulative gas production between the different degrees of thermal effects during 30 years of production. (b) Comparison of the stress-affected permeability of the PF between the different degrees of thermal effects during 30 years of production. (c) Comparison of the stress-dependent permeability of the SRD between the different degrees of thermal effects during 30 years of production. (d) Comparison of the stress-dependent permeability of the NSRD between the different degrees of thermal effects during 30 years of production.

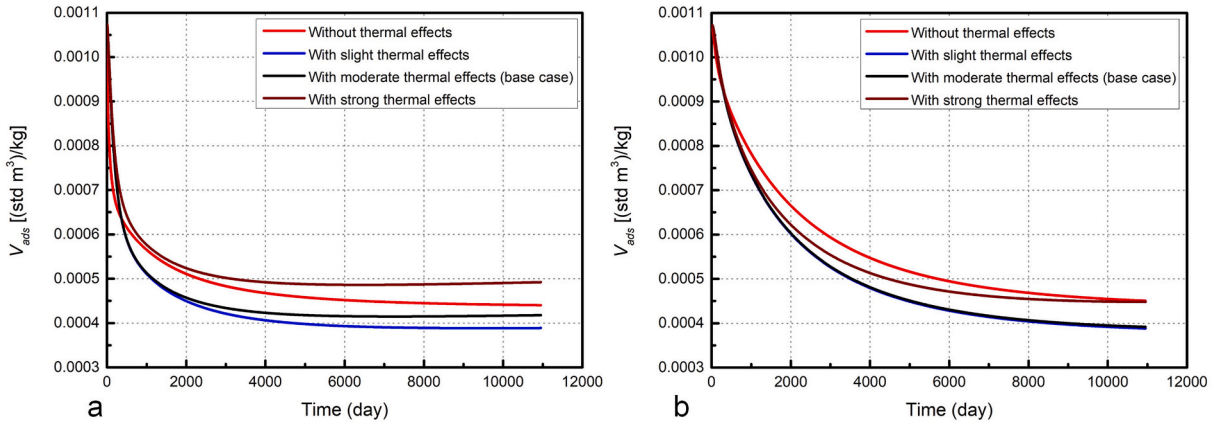

Fig. 20. Influences of the different degrees of thermal effects on the adsorbed gas amount evolution. (a) Evolution of V_{ads} with the different degrees of thermal effects in the SRD during 30 years of production. (b) Evolution of V_{ads} with the different degrees of thermal effects in the NSRD during 30 years of production.

influences caused by thermal effects not only competitively impact gas production but also competitively impact the different production periods to varying degrees. Among the three cases with different degrees of thermal effects, during the early period, thermal-shrinkage-strain-induced permeability enhancement played an important role in improving gas production, while with increasing gas depletion, the hindrance effect caused by non-isothermal desorption on gas production would become increasingly more significant. This suggests that selecting an appropriate shutdown time to terminate CBM extraction is of significance. Considering the possible hindrance effect of temperature reduction (during the late period) on gas desorption and the fact that a considerable fraction of the total CBM storage volume is adsorbed gas, a too-long production time may not suitably realize the most cost-effective extraction. Compared to the isothermal CBM extraction models introduced in previous studies, the difference attributed to the added physical factors/processes considering thermal effects

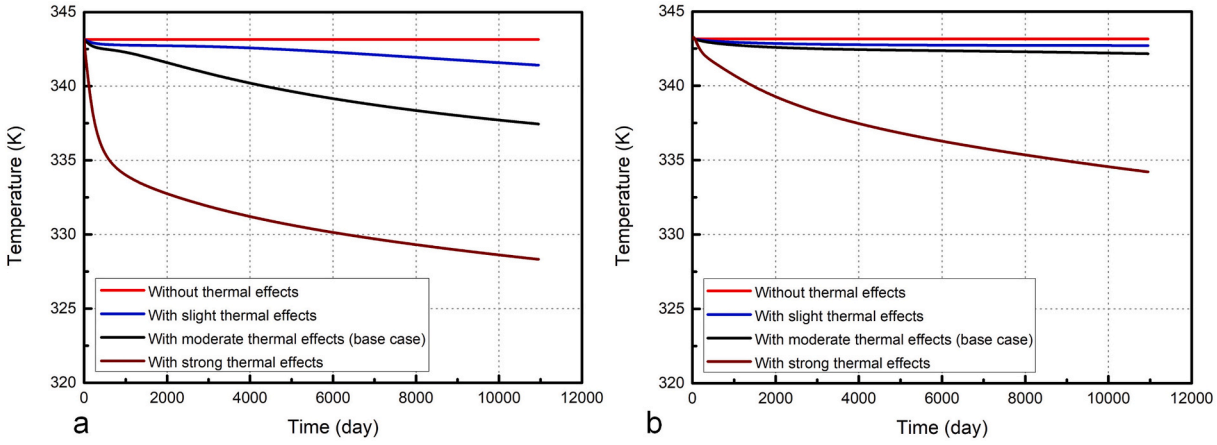

Fig. 21. Influences of the different degrees of thermal effects on temperature evolution. (a) Evolution of the temperature with the different degrees of thermal effects in the SRD during 30 years of production. (b) Evolution of the temperature with the different degrees of thermal effects in the NSRD during 30 years of production.

Table 6
Added physical factors/processes in the proposed model considering thermal effects compared to isothermal CBM extraction models (note: both T and p decrease during CBM extraction).

Added factors/processes in the proposed model compared to isothermal models	Difference in the simulation results between the proposed model and isothermal models	Effect of considering the added factors/processes on gas production
Thermal strain	Enhanced stress-dependent porosity and permeability	Positive
Non-isothermal desorption amount	Lower gas supply by desorption because of temperature reduction	Negative
Non-isothermal desorption strain	Smaller change in desorption strain	Negative
Gas density change with the temperature	Difference in gas density computed with the equation of state	Determined by the coupling computation

in this work and their meanings for gas recovery improvement are summarized in Table 6. These additional factors/processes are fully coupled with other physical processes in the proposed model to accurately predict CBM production.

In summary, a comprehensive investigation was carried out by applying the proposed multidomain and multiphysics (THM coupled) model in this section to deepen the understanding of the effects of the key influencing factors on CBM extraction. In Section 5.1, we focused on the multidomain effects and obtained the following findings: first, to maximize the improvement effect of stimulation treatments on gas production, the complexity of fractures should be intensified as much as possible to generate a combination of PFs and SRD instead of a single kind of fracture. Second, enlarging the SRD size and enhancing the initial permeability of the SRD/PF is vital to enhance the CBM recovery. Third, with the global mechanical coupling relationship, a change occurring in one domain simultaneously affects the property evolution trends in the other domains, which in turn influences the mass transfer efficiency and resultant CBM production. In Section 5.2, we investigated the thermal effects and obtained the following findings: first, energy loss accompanies gas depletion, resulting in a temperature decrease in the CBM reservoir. The temperature decrease in the SRD is more significant than that in the NSRD. Second, if the thermal effects are ignored, the CBM production and variable permeability may be overestimated because of the overestimation of sorption-induced strain or may be underestimated due to not considering thermal strain. Third, the temperature reduction attributed to heat transfer affects the non-isothermal adsorption balance and results in less extractable adsorbed gas. The various influences of thermal effects not only competitively impact gas production but also competitively impact the different periods of production to varying extents. These findings, along with the proposed model, update the existing understanding of evolving CBM reservoirs and guide the engineering design of CBM extraction.

6. Conclusions

In this work, a fully coupled multidomain and multiphysics (thermal-hydraulic-mechanical) model was developed and verified to simulate gas extraction in coalbed methane (CBM) reservoirs with various stimulation patterns. Multiple physical processes, including gas flow, coal deformation, heat transfer, and non-isothermal sorption in each domain (stimulated reservoir domain—SRD; non-stimulated reservoir domain—NSRD; and radial primary fracture—PF), were modelled, while the interactions among these processes/domains were incorporated into the model via cross-coupling relationships. In particular, the description of thermal shrinkage, non-isothermal sorption, and non-isothermal gas density change within the multidomain framework including the PF, SRD, and NSRD, during CBM extraction represented the main novelty of the proposed model. The PDEs of the proposed model were numerically solved with the finite element method and verified against field observations. Comparison of the proposed model and previously published models revealed the great accuracy of the proposed model. A comprehensive investigation was carried out by applying the proposed model to evaluate the effects of key influencing factors on CBM extraction. In this work, we not only bridged the technical gap between describing stimulated (single-domain) and unstimulated (multidomain) CBM reservoirs but we also bridged the knowledge gap in understanding CBM extraction in multidomain CBM reservoirs with/without thermal effects.

According to the modelling and simulation results, the following specific conclusions can be drawn:

(1) The contrast in properties of the PF, SRD, and NSRD in stimulated CBM reservoirs leads to different property evolution trends in these domains, which in turn controls the effectiveness of gas extraction. It is crucial to select appropriate stimulation techniques to improve the complexity of fractures, enlarge the SRD size, and increase the PF and SRD permeabilities to enhance the CBM recovery.
(2) The multidomain mechanical coupling relationship links the changes in the stress-dependent porosity and permeability in the different domains of CBM reservoirs. With this linkage, a change occurring in one domain simultaneously affects the property evolutions in the other domains, influencing the mass transfer efficiency and resultant CBM production.

(3) Simultaneous reduction in the temperature and pressure during CBM extraction leads to multiple competitive effects on the evolution of the stress-dependent porosity/permeability, desorption amount, and gas density. These effects, playing varying roles during the different periods of CBM extraction, impose various influences on cumulative gas production. Ignoring thermal effects may result in overestimation or underestimation of gas production, which mainly depends on the net effects of thermal shrinkage strain and non-isothermal desorption.

Credit author statement

Wai Li: Conceptualization, literature review, investigation, methodology, writing – original draft preparation. **Jishan Liu**: Supervision, resource, writing – reviewing and editing. **Jie Zeng**: Data curation; methodology, writing – draft revision. **Yee-Kwong Leong**: Supervision, resource. **Derek Elsworth**: Supervision, resource. **Jianwei Tian**: Literature review, investigation.

Declaration of competing interest

The authors declare that they have no known competing financial interests or personal relationships that could have appeared to influence the work reported in this paper.

Acknowledgements

The authors gratefully acknowledge the financial support received from the Australian Government Research Training Program (RTP) scholarship and the Australian Research Council (Grant No. DP200101293). Parts of this work were completed to fulfil the Ph.D. degree requirements of Wai Li at the University of Western Australia.

References

An, F., Cheng, Y., Wang, L., Li, W., 2013. A numerical model for outburst including the effect of adsorbed gas on coal deformation and mechanical properties. Comput. Geotech. 54, 222–231. https://doi.org/10.1016/j.compgeo.2013.07.013.

Atkins, P., Atkins, P.W., de Paula, J., 2014. Atkins' physical chemistry. Oxford university press.

Bai, M., Elsworth, D., 2000. Coupled Processes in Subsurface Deformation, Flow, and Transport. ASCE Press. https://doi.org/10.1061/9780784404607.

Bai, M., Elsworth, D., Inyang, H.I., Roegiers, J.C., 1997. Modeling contaminant migration with linear sorption in strongly heterogeneous media. J. Environ. Eng. 123, 1116–1125. https://doi.org/10.1061/(ASCE)0733-9372(1997)123:11(1116).

Barenblatt, G.I., Zheltov, I.P., Kochina, I.N., 1960. Basic concepts in the theory of seepage of homogeneous liquids in fissured rocks [strata]. J. Appl. Math. Mech. 24, 1286–1303. https://doi.org/10.1016/0021-8928(60)90107-6.

Berryman, J.G., 2002. Extension of poroelastic analysis to double-porosity materials: new technique in microgeomechanics. J. Eng. Mech. 128, 840–847. https://doi.org/10.1061/(ASCE)0733-9399(2002)128:8(840).

Brown, M., Ozkan, E., Raghavan, R., Kazemi, H., 2011. Practical solutions for pressure-transient responses of fractured horizontal wells in unconventional shale reservoirs. SPE Reservoir Eval. Eng. 14, 663–676. https://doi.org/10.2118/125043-PA.

Busch, A., Gensterblum, Y., 2011. CBM and CO_2-ECBM related sorption processes in coal: a review. Int. J. Coal Geol. 87, 49–71. https://doi.org/10.1016/j.coal.2011.04.011.

Cao, P., Liu, J., Leong, Y.K., 2016a. A fully coupled multiscale shale deformation-gas transport model for the evaluation of shale gas extraction. Fuel 178, 103–117. https://doi.org/10.1016/j.fuel.2016.03.055.

Cao, P., Liu, J., Leong, Y.K., 2016b. General gas permeability model for porous media: bridging the gaps between conventional and unconventional natural gas reservoirs. Energy Fuel. 30, 5492–5505. https://doi.org/10.1021/acs.energyfuels.6b00683.

Cao, P., Liu, J., Leong, Y.K., 2017b. A multiscale-multiphase simulation model for the evaluation of shale gas recovery coupled the effect of water flowback. Fuel 199, 191–205. https://doi.org/10.1016/j.fuel.2017.02.078.

Cao, Y., Zhang, J., Zhai, H., Fu, G., Tian, L., Liu, S., 2017a. CO_2 gas fracturing: a novel reservoir stimulation technology in low permeability gassy coal seams. Fuel 203, 197–207. https://doi.org/10.1016/j.fuel.2017.04.053.

Chen, Z., Liao, X., Zhao, X., Dou, X., Zhu, L., 2016. A semi-analytical mathematical model for transient pressure behavior of multiple fractured vertical well in coal reservoirs incorporating with diffusion, adsorption, and stress-sensitivity. J. Nat. Gas Sci. Eng. 29, 570–582. https://doi.org/10.1016/j.jngse.2015.08.043.

Chen, Z., Liu, J., Kabir, A., Wang, J., Pan, Z., 2013. Impact of various parameters on the production of coalbed methane. SPE J. 18, 910–923. https://doi.org/10.2118/162722-PA.

Clarkson, C.R., Bustin, R.M., Seidle, J.P., 2007. Production-data analysis of single-phase (gas) coalbed-methane wells. SPE Reservoir Eval. Eng. 10, 312–331. https://doi.org/10.2118/100313-PA.

Clarkson, C.R., McGovern, J.M., 2005. Optimization of Coalbed-Methane-Reservoir Exploration and Development Strategies through Integration of Simulation and Economics, vol. 8. SPE Reservoir Evaluation & Engineering, pp. 502–519. https://doi.org/10.2118/88843-PA.

Craig, D.P., Blasingame, T.A., 2006. Constant-rate drawdown solutions derived for multiple arbitrarily oriented uniform-flux, infinite-conductivity, or finite-conductivity fractures in an infinite-slab reservoir. In: Presented at the SPE Gas Technology Symposium, Calgary, Alberta, Canada, May 15–17. https://doi.org/10.2118/100586-MS.

Cui, G., Liu, J., Wei, M., Shi, R., Elsworth, D., 2018. Why shale permeability changes under variable effective stresses: new insights. Fuel 213, 55–71. https://doi.org/10.1016/j.fuel.2017.10.068.

Cui, G., Tan, Y., Chen, T., Feng, X.T., Elsworth, D., Pan, Z., Wang, C., 2020. Multidomain two-phase flow model to study the impacts of hydraulic fracturing on shale gas production. Energy Fuel. 34, 4273–4288. https://doi.org/10.1021/acs.energyfuels.0c00062.

Cui, X., Bustin, R.M., 2005. Volumetric strain associated with methane desorption and its impact on coalbed gas production from deep coal seams. AAPG (Am. Assoc. Pet. Geol.) Bull. 89, 1181–1202. https://doi.org/10.1306/05110504114.

Deng, J., Kang, J., Zhou, F., Li, H., Zhang, D., Li, G., 2019. The adsorption heat of methane on coal: comparison of theoretical and calorimetric heat and model of heat flow by microcalorimeter. Fuel 237, 81–90. https://doi.org/10.1016/j.fuel.2018.09.123.

Detournay, E., Cheng, A.H.D., 1993. Fundamentals of Poroelasticity. Pergamon, Oxford, pp. 113–171. https://doi.org/10.1016/B978-0-08-040615-2.50011-3.

Dunne, J.A., Mariwala, R., Rao, M., Sircar, S., Gorte, R.J., Myers, A.L., 1996. Calorimetric heats of adsorption and adsorption isotherms. 1. O_2, N_2, Ar, CO_2, CH_4, C_2H_6, and SF_6 on silicalite. Langmuir 12, 5888–5895. https://doi.org/10.1021/la960495z.

Elsworth, D., Bai, M., 1992. Flow-deformation response of dual-porosity media. J. Geotech. Eng. 118, 107–124. https://doi.org/10.1061/(ASCE)0733-9410(1992)118:1(107).

Fan, C., Elsworth, D., Li, S., Chen, Z., Luo, M., Song, Y., Zhang, H., 2019. Modelling and optimization of enhanced coalbed methane recovery using CO_2/N_2 mixtures. Fuel 253, 1114–1129. https://doi.org/10.1016/j.fuel.2019.04.158.

Fan, Y., Deng, C., Zhang, X., Li, F., Wang, X., Qiao, L., 2018. Numerical study of CO_2-enhanced coalbed methane recovery. Int. J. Greenh. Gas Control 76, 12–23. https://doi.org/10.1016/j.ijggc.2018.06.016.

Gao, Q., Cheng, Y., Han, S., Yan, C., Jiang, L., 2019. Numerical modeling of hydraulic fracture propagation behaviors influenced by pre-existing injection and production wells. J. Petrol. Sci. Eng. 172, 976–987. https://doi.org/10.1016/j.petrol.2018.09.005.

Gentzis, T., Bolen, D., 2008. The use of numerical simulation in predicting coalbed methane producibility from the gates coals, alberta inner foothills, Canada: comparison with mannville coal CBM production in the alberta syncline. Int. J. Coal Geol. 74, 215–236. https://doi.org/10.1016/j.coal.2007.12.003.

Germanovich, L.N., Ring, L.M., Astakhov, D.K., Shlyapobersky, J., Mayerhofer, M.J., 1997. Hydraulic fracture with multiple segments II. Modeling. Int. J. Rock Mech. Min. Sci. 34 https://doi.org/10.1016/S1365-1609(97)00079-8, 98.e1–98.e15.

Jurus, W.J., Whitson, C.H., Golan, M., 2013. Modeling water flow in hydraulically-fractured shale wells. In: Presented at the SPE Annual Technical Conference and Exhibition. New Orleans, Louisiana, September 30–October 2. https://doi.org/10.2118/166439-MS.

Kou, Z., Wang, H., 2020. Transient pressure analysis of a multiple fractured well in a stress-sensitive coal seam gas reservoir. Energies 13, 3849. https://doi.org/10.3390/en13153849.

Kranz, R.L., Saltzman, J.S., Blacic, J.D., 1990. Hydraulic diffusivity measurements on laboratory rock samples using an oscillating pore pressure method. Int. J. Rock Mech. Min. Sci. 27, 345–352. https://doi.org/10.1016/0148-9062(90)92709-N.

Li, S., Fan, C., Han, J., Luo, M., Yang, Z., Bi, H., 2016. A fully coupled thermal-hydraulic-mechanical model with two-phase flow for coalbed methane extraction. J. Nat. Gas Sci. Eng. 33, 324–336. https://doi.org/10.1016/j.jngse.2016.05.032.

Li, W., Liu, J., Zeng, J., Leong, Y.K., Elsworth, D., 2019b. A fully coupled multidomain and multiphysics model for shale gas production. In: Presented at the 5th ISRM Young Scholars' Symposium on Rock Mechanics and International Symposium on Rock Engineering for Innovative Future, Okinawa, Japan, December 1–4. In: https://onepetro.org/ISRMYSS/proceedings-abstract/YSRM19/All-YSRM19/ISRM-YSRM-2019-063/445862.

Li, W., Liu, J., Zeng, J., Leong, Y.K., Elsworth, D., Tian, J., Li, L., 2020b. A fully coupled multidomain and multiphysics model for evaluation of shale gas extraction. Fuel 278, 118214. https://doi.org/10.1016/j.fuel.2020.118214.

Li, W., Liu, J., Zeng, J., Tian, J., Li, L., Zhang, M., Jia, J., Li, Y., Peng, H., Zhao, X., Jiang, J., 2019a. A critical review of the application of nanomaterials in frac fluids: the state of the art and challenges. In: Presented at the SPE Middle East Oil and Gas Show and Conference. Manama, Bahrain, March 18–21. https://doi.org/10.2118/195029-MS.

Li, Z.X., Liu, J.Y., Luo, D.K., Wang, J.J., 2020a. Study of evaluation method for the overseas oil and gas investment based on risk compensation. Petrol. Sci. 17, 858–871. https://doi.org/10.1007/s12182-020-00457-7.

Lim, K.T., Aziz, K., 1995. Matrix-fracture transfer shape factors for dual-porosity simulators. J. Petrol. Sci. Eng. 13, 169–178. https://doi.org/10.1016/0920-4105(95)00010-F.

Liu, G., Liu, J., Liu, L., Ye, D., Gao, F., 2019. A fractal approach to fully-couple coal deformation and gas flow. Fuel 240, 219–236. https://doi.org/10.1016/j.fuel.2018.11.140.

Liu, H., Cheng, Y., 2015. The elimination of coal and gas outburst disasters by long distance lower protective seam mining combined with stress-relief gas extraction in the Huaibei coal mine area. J. Nat. Gas Sci. Eng. 27, 346–353. https://doi.org/10.1016/j.jngse.2015.08.068.

Liu, H., Liu, H., Cheng, Y., 2014a. The elimination of coal and gas outburst disasters by ultrathin protective seam drilling combined with stress-relief gas drainage in Xinggong Coalfield. J. Nat. Gas Sci. Eng. 21 https://doi.org/10.1016/j.jngse.2014.10.022, 873–844.

Liu, J., Chen, Z., Elsworth, D., Miao, X., Mao, X., 2010. Linking gas-sorption induced changes in coal permeability to directional strains through a modulus reduction ratio. Int. J. Coal Geol. 83, 21–30. https://doi.org/10.1016/j.coal.2010.04.006.

Liu, J., Chen, Z., Elsworth, D., Qu, H., Chen, D., 2011. Interactions of multiple processes during CBM extraction: a critical review. Int. J. Coal Geol. 87, 175–189. https://doi.org/10.1016/j.coal.2011.06.004.

Liu, J., Elsworth, D., Brady, B.H., 1999. Linking stress-dependent effective porosity and hydraulic conductivity fields to RMR. Int. J. Rock Mech. Min. Sci. 36, 581–596. https://doi.org/10.1016/S0148-9062(99)00029-7.

Liu, J., Liu, Z., Gao, K., Ma, Y.K., Li, Z.Q., Guo, L.J., 2014b. Experimental study and application of directional focused energy blasting in deep boreholes. Chin. J. Rock Mech. Eng. 33, 2490–2496. https://doi.org/10.13722/j.cnki.jrme.2014.12.014.

Luo, W., Tang, C., 2015. Pressure-transient analysis of multiwing fractures connected to a vertical wellbore. SPE J. 20, 360–367. https://doi.org/10.2118/171556-PA.

Liu, X., Sheng, J., Liu, J., Hu, Y., 2018. Evolution of coal permeability during gas injection—from initial to ultimate equilibrium. Energies 11 (10), 2800. https://doi.org/10.3390/en11102800.

Mahmoud, M., 2014. Development of a new correlation of gas compressibility factor (Z-factor) for high pressure gas reservoirs. J. Energy Resour. Technol. 136, 012903 https://doi.org/10.1115/1.4025019.

Mehrabian, A., Abousleiman, Y.N., 2015. Gassmann equations and the constitutive relations for multiple-porosity and multiple-permeability poroelasticity with applications to oil and gas shale. Int. J. Numer. Anal. Methods GeoMech. 39, 1547–1569. https://doi.org/10.1002/nag.2399.

Palmer, I., Mansoori, J., 1998. How Permeability Depends on Stress and Pore Pressure in Coalbeds: A New Model, vol. 1. SPE Reservoir Evaluation & Engineering, pp. 539–544. https://doi.org/10.2118/52607-PA.

Pan, Z., Connell, L.D., 2012. Modelling permeability for coal reservoirs: a review of analytical models and testing data. Int. J. Coal Geol. 92, 1–44. https://doi.org/10.1016/j.coal.2011.12.009.

Peng, Y., Liu, J., Pan, Z., Connell, L.D., 2015. A sequential model of shale gas transport under the influence of fully coupled multiple processes. J. Nat. Gas Sci. Eng. 27, 808–821. https://doi.org/10.1016/j.jngse.2015.09.031.

Peng, Y., Liu, J., Wei, M., Pan, Z., Connell, L.D., 2014. Why coal permeability changes under free swellings: new insights. Int. J. Coal Geol. 133, 35–46. https://doi.org/10.1016/j.coal.2014.08.011.

Qu, H., Liu, J., Chen, Z., Wang, J., Pan, Z., Connell, L., Elsworth, D., 2012. Complex evolution of coal permeability during CO_2 injection under variable temperatures. Int. J. Greenh. Gas Control 9, 281–293. https://doi.org/10.1016/j.ijggc.2012.04.003.

Rezaee, R., 2015. Fundamentals of Gas Shale Reservoirs, first ed. John Wiley & Sons, New Jersey.

Sakhaee-Pour, A., Bryant, S., 2012. Gas Permeability of Shale, vol. 15. SPE Reservoir Evaluation & Engineering, pp. 401–409. https://doi.org/10.2118/146944-PA.

Settari, A., Cleary, M.P., 1984. Three-dimensional simulation of hydraulic fracturing. J. Petrol. Technol. 36, 1177–1190. https://doi.org/10.2118/10504-PA.

Shi, J.Q., Durucan, S., 2004. Drawdown induced changes in permeability of coalbeds: a new interpretation of the reservoir response to primary recovery. Transport Porous Media 56, 1–16. https://doi.org/10.1023/B:TIPM.0000018398.19928.5a.

Shi, J.T., Wu, J.Y., Sun, Z., Xiao, Z.H., Liu, C., Sepehrnoori, K., 2020. Methods for simultaneously evaluating reserve and permeability of undersaturated coalbed methane reservoirs using production data during the dewatering stage. Petrol. Sci. 17, 1067–1086. https://doi.org/10.1007/s12182-019-00410-3.

Sun, Z., Shi, J., Zhang, T., Wu, K., Feng, D., Sun, F., Huang, L., Hou, C., Li, X., 2018. A fully-coupled semi-analytical model for effective gas/water phase permeability during coal-bed methane production. Fuel 223, 44–52. https://doi.org/10.1016/j.fuel.2018.03.012.

Teng, T., Zhao, Y., Gao, F., Wang, J.G., Wang, W., 2018. A fully coupled thermo-hydro-mechanical model for heat and gas transfer in thermal stimulation enhanced coal seam gas recovery. Int. J. Heat Mass Tran. 125, 866–875. https://doi.org/10.1016/j.ijheatmasstransfer.2018.04.112.

Tian, J., Liu, J., Elsworth, D., Leong, Y.K., Li, W., Zeng, J., 2019. A dynamic fractal permeability model for heterogeneous coalbed reservoir considering multiphysics and flow regimes. In: Presented at the SPE/AAPG/SEG Unconventional Resources Technology Conference, Denver, Colorado, USA, July 22–24. https://doi.org/10.15530/urtec-2019-250.

Van Heel, A.P.G., Boerrigter, P.M., van Dorp, J.J., 2008. Thermal and Hydraulic Matrix-Fracture Interaction in Dual-Oermeability Simulation, vol. 11. SPE Reservoir Evaluation & Engineering, pp. 735–749. https://doi.org/10.2118/102471-PA.

Vishal, V., Singh, T.N., Ranjith, P.G., 2015. Influence of sorption time in CO_2-ECBM process in indian coals using coupled numerical simulation. Fuel 139, 51–58. https://doi.org/10.1016/j.fuel.2014.08.009.

Warren, J.E., Root, P.J., 1963. The behavior of naturally fractured reservoirs. Soc. Petrol. Eng. J. 3, 245–255. https://doi.org/10.2118/426-PA.

Wei, C., Qin, Y., Wang, G.G.X., Fu, X., 2010. Numerical simulation of coalbed methane generation, dissipation and retention in SE edge of Ordos Basin, China. Int. J. Coal Geol. 82, 147–159. https://doi.org/10.1016/j.coal.2009.12.005.

Wei, M., Liu, J., Elsworth, D., Wang, E., 2018. Triple-porosity modelling for the simulation of multiscale flow mechanisms in shale reservoirs. Geofluids 6948726. https://doi.org/10.1155/2018/6948726, 2018.

Wei, M.Y., Liu, J., Liu, Y.K., Liu, Z.H., Elsworth, D., 2021. Effect of adsorption-induced matrix swelling on coal permeability evolution of micro-fracture with the real geometry. Petrol. Sci. 18, 1143–1152. https://doi.org/10.1016/j.petsci.2021.07.006.

Wu, Y., Liu, J., Elsworth, D., Chen, Z., Connell, L., Pan, Z., 2010a. Dual poroelastic response of a coal seam to CO_2 injection. Int. J. Greenh. Gas Control 4, 668–678. https://doi.org/10.1016/j.ijggc.2010.02.004.

Wu, Y., Liu, J., Elsworth, D., Miao, X., Mao, X., 2010b. Development of anisotropic permeability during coalbed methane production. J. Nat. Gas Sci. Eng. 2, 197–210. https://doi.org/10.1016/j.jngse.2010.06.002.

Xia, L., Yin, Y., Yu, X., Zheng, Y., 2019. An approach to grading coalbed methane resources in China for the purpose of implementing a differential production subsidy. Petrol. Sci. 16, 447–457. https://doi.org/10.1007/s12182-019-0303-0.

Xia, T., Zhou, F., Gao, F., Kang, J., Liu, J., Wang, J., 2015. Simulation of coal self-heating processes in underground methane-rich coal seams, 141–142: 1–12 Int. J. Coal Geol.. https://doi.org/10.1016/j.coal.2015.02.007.

Xia, T., Zhou, F., Liu, J., Hu, S., Liu, Y., 2014. A fully coupled coal deformation and compositional flow model for the control of the pre-mining coal seam gas extraction. Int. J. Rock Mech. Min. Sci. 72, 138–148. https://doi.org/10.1016/j.ijrmms.2014.08.012.

Yuan, B., Su, Y., Moghanloo, R.G., Rui, Z., Wang, W., Shang, Y., 2015. A new analytical multi-linear solution for gas flow toward fractured horizontal wells with different fracture intensity. J. Nat. Gas Sci. Eng. 23, 227–238. https://doi.org/10.1016/j.jngse.2015.01.045.

Zeng, J., Li, W., Liu, J., Leong, Y.K., Elsworth, D., Tian, J., Guo, J., Zeng, F., 2020a. Analytical solutions for multi-stage fractured shale gas reservoirs with damaged fractures and stimulated reservoir volumes. J. Petrol. Sci. Eng. 187, 106686. https://doi.org/10.1016/j.petrol.2019.106686.

Zeng, J., Liu, J., Li, W., Leong, Y.K., Elsworth, D., Guo, J., 2021. Shale gas reservoir modeling and production evaluation considering complex gas transport mechanisms and dispersed distribution of kerogen. Petrol. Sci. 18, 195–218. https://doi.org/10.1007/s12182-020-00495-1.

Zeng, J., Liu, J., Li, W., Leong, Y.K., Elsworth, D., Guo, J., 2020b. Evolution of shale permeability under the influence of gas diffusion from the fracture wall into the matrix. Energy Fuel. 34, 4393–4406. https://doi.org/10.1021/acs.energyfuels.0c00219.

Zeng, J., Liu, J., Li, W., Tian, J., Leong, Y.K., Elsworth, D., Guo, J., 2019. Impact of swelling area expansion from the fracture wall into the matrix on the evolution of coal permeability. In: Presented at the 5th ISRM Young Scholars' Symposium on Rock Mechanics and International Symposium on Rock Engineering for Innovative Future, Okinawa, Japan, December 1–4. In: https://onepetro.org/ISRMYSS/proceedings-abstract/YSRM19/All-YSRM19/ISRM-YSRM-2019-021/445823.

Zhang, H., Liu, J., Elsworth, D., 2008. How sorption-induced matrix deformation affects gas flow in coal seams: a new FE model. Int. J. Rock Mech. Min. Sci. 45, 1226–1236. https://doi.org/10.1016/j.ijrmms.2007.11.007.

Zhang, J., Si, L., Chen, J., Kizil, M., Wang, C., Chen, Z., 2020b. Stimulation techniques of coalbed methane reservoirs. Geofluids 5152646. https://doi.org/10.1155/2020/5152646, 2020.

Zhang, L., Kou, Z., Wang, H., Zhao, Y., Dejam, M., Guo, J., Du, J., 2018. Performance analysis for a model of a multi-wing hydraulically fractured vertical well in a coalbed methane gas reservoir. J. Petrol. Sci. Eng. 166, 104–120. https://doi.org/10.1016/j.petrol.2018.03.038.

Zhang, X., Zhang, S., Yang, Y., Zhang, P., Wei, G., 2016. Numerical simulation by hydraulic fracturing engineering based on fractal theory of fracture extending in the coal seam. J. Natl. Gas Geosci. 1, 319–325. https://doi.org/10.1016/j.jnggs.2016.08.006.

Zhang, Z., Liu, Y., Sun, H., Xiong, W., Shen, K., Ba, Q., 2020a. An alternative approach to match field production data from unconventional gas-bearing systems. Petrol. Sci. 17, 1370–1388. https://doi.org/10.1007/s12182-020-00454-w.

Zhu, W., Wei, C., Wei, J., Yang, T., 2012. Numerical simulation on gas flow in coal seam enhanced by controlled blasting. In: Presented at the ISRM Regional Symposium - 7th Asian Rock Mechanics Symposium, Seoul, Korea, October 15–19. https://www.onepetro.org/conference-paper/ISRM-ARMS7-2012-033.

Zhu, W.C., Wei, C.H., Liu, J., Qu, H.Y., Elsworth, D., 2011. A model of coal–gas interaction under variable temperatures. Int. J. Coal Geol. 86, 213–221. https://doi.org/10.1016/j.coal.2011.01.011.